Search for New Physics through the Observables of Semileptonic $B_c^+ \to D^{*+}\ell^+\ell^-$ Decay

Zohaib Aarfi[1†] Qazi Maaz Us Salam[2,3‡] Faisal Munir Bhutta[1§] Ishtiaq Ahmed[3¶] M. Ali Paracha[1♯]

[1]Department of Physics and Astronomy, School of Natural Sciences, National University of Sciences and Technology (NUST), H-12, Islamabad 44000, Pakistan
[2]Department of Physics, Lahore University of Management Sciences (LUMS), Opposite Sector U, D.H.A, Lahore 54792, Pakistan
[3]National Centre for Physics, Shahdra Valley Road, Islamabad 45320, Pakistan

Abstract: Motivated by current flavor anomalies and by the relatively unexplored nature of the $b \to d$ sector, we present a model-independent study of the rare semileptonic decay $B_c^+ \to D^{*+}\ell^+\ell^-$ $(\ell = \mu, \tau)$ to investigate its sensitivity to New Physics effects. The analysis incorporates penguin--box contributions, long-distance resonance effects, and substantial weak-annihilation amplitudes. Using the $B_c \to D^*$ transition form factors calculated in the covariant confined quark model and the weak-annihilation form factors obtained within the Bethe--Salpeter approach, we analyze the differential branching fraction, forward-backward asymmetry, longitudinal helicity fraction, and a comprehensive set of normalized angular observables in several one- and two-dimensional New Physics scenarios. We compare these results with the corresponding Standard Model predictions. Notably, the branching fraction, forward-backward asymmetry, and normalized angular coefficients, including $\langle I_{2c}\rangle$, $\langle I_3\rangle$, $\langle I_5\rangle$, and $\langle I_{6s}\rangle$, show clear sensitivity to New Physics effects. Our results indicate that the decay $B_c^+ \to D^{*+}\ell^+\ell^-$ serves as a complementary probe of the flavor structure of New Physics and can therefore be investigated in future measurements at LHCb and other high-luminosity flavor experiments.

DOI: **CSTR:**

CPC Accepted

I. INTRODUCTION

In the framework of the Standard Model (SM), the rare semileptonic $B_c^+ \to D^{*+}\ell^+\ell^-$, $(\ell = \mu, \tau)$ decays are mediated by the flavor-changing neutral current (FCNC) $b \to d$ transition. The dominant contribution to these processes originates from an internal top-quark loop, in which the large top-quark mass enhances the virtual effects. The branching ratio for this transition is highly suppressed, reaching the order of $O(10^{-8})$, primarily because it is a loop-induced FCNC process and also because of the small magnitude of the CKM matrix element V_{td} [1, 2]. Although this suppression makes these decays sensitive probes of new physics (NP), they are also theoretically interesting because CP violation in the $b \to d$ transition is significantly larger than in the $b \to s$ transition.

Interest in FCNC rare decays, particularly those driven by $b \to s\ell^+\ell^-$ transitions, has increased significantly following the observation of flavor anomalies. Although high-precision measurements from the LHCb collaboration show that the lepton flavor universality (LFU) ratios $R_{K^{(*)}}$ are consistent with SM predictions [3], the angular observable P_5' continues to exhibit a deviation from the SM with an approximate significance of $2.5\sigma - 3.0\sigma$ [4], and the branching fraction of the $B_s \to \phi\mu^+\mu^-$ decay deviates by about 3.6σ from the SM prediction [5]. These anomalies suggest that the flavor sector may still be influenced by NP and motivate the exploration of NP through decays mediated by the $b \to d$ transition as a complementary test. Furthermore, investigating $b \to d$ transitions allows us to test whether potential NP effects originate from new sources of flavor symmetry breaking. Since these transitions are more Cabibbo-suppressed than $b \to s$ processes, they offer a unique window in which NP contributions might be more discernible.

Experimentally, several measurements and upper bounds for rare $b \to d$ channels have already been reported by the LHCb, BaBaR, and Belle collaborations, including $B^+ \to \pi^+\mu^+\mu^-$, $B^0 \to \pi^+\pi^-\mu^+\mu^-$, and $B^0 \to \rho^0\mu^+\mu^-$ [6–9]. Recently, Belle extended these searches to the modes $B \to (\pi, \eta, \rho, \omega)\ell^+\ell^-$ and set upper limits at the level

Received 30 June 2026; Accepted 26 October 2026
† E-mail: zohaib.phdphy22sns@student.nust.edu.pk
‡ E-mail: qazimaaz92@gmail.com
§ E-mail: faisal.munir@sns.nust.edu.pk
¶ E-mail: ishtiaq.ahmed@ncp.edu.pk
♯ E-mail: aliparacha@sns.nust.edu.pk (corresponding author)

©2026 Chinese Physical Society and the Institute of High Energy Physics of the Chinese Academy of Sciences and the Institute of Modern Physics of the Chinese Academy of Sciences and IOP Publishing Ltd. All rights, including for text and data mining, AI training, and similar technologies, are reserved.

of $(3.8-47)\times10^{-8}$ [10]. Furthermore, evidence for the decay $B_s \to \bar{K}^*\mu^+\mu^-$, with a branching fraction of $(2.9\pm1.1)\times10^{-8}$ [11], has been reported by LHCb. Upcoming data from current and future collider experiments are expected to improve the sensitivity to these suppressed modes and enable precision measurements of the observables associated with these decays [12].

In this context, the B_c meson provides a unique laboratory for testing the SM. Its decay dynamics provide information complementary to that from the $B_{u,d,s}$ systems [13−20]. Furthermore, owing to the large production cross section of the B_c meson at the LHC, several hadronic and semileptonic B_c decay channels have been established [21−26], providing a valuable setting for testing SM parameters as well as NP. These developments motivate us to study NP through semileptonic $B_c \to D^{(*)}_{s,d}\ell^+\ell^-$ decays, which offer a rich set of physical observables for analyzing NP effects. One important feature of $B_c \to D^{(*)}_{s,d}\ell^+\ell^-$ decays that distinguishes them from other $B_{u,s,d}$ decays is the significant role of the weak annihilation (WA) contribution. In B_c decays, the penguin-box (PB) and WA contributions enter on an equal footing because the associated CKM matrix elements have comparable magnitudes. In the literature, the decays $B_c \to D^*_{s,d}\ell^+\ell^-$ have been studied within both the SM and different NP models [27−39].

In this work, we investigate the decays $B_c^+ \to D^{*+}(\to P_1P_2)\ell^+\ell^-$, with $P_1P_2 = D^+\pi^0, D^0\pi^+$, and $\ell = \mu,\tau$, in a model-independent NP framework. This study is a natural extension of our previous work [40], in which we analyzed the impact of WA, PB, and long-distance (LD) contributions within the SM. The impact of NP can be probed using the differential branching ratio, forward-backward (FB) asymmetry, longitudinal helicity fraction of the final-state D^* meson, and angular coefficients I_i. The PB form factors used to analyze the physical observables were computed in the framework of the covariant confined quark model (CCQM) [41], and the form factors associated with the WA amplitude were computed numerically using the Bethe–Salpeter (BS) approach [42]. A comparison of the form factors obtained from the relativistic quark model, light-front approach, and pQCD was made in [41]. Another comparison between the CCQM form factors [41] and recent pQCD form factors [43] was presented in our previous work [40]. In a study based on three-point QCD sum rules [44], the authors predicted noticeably smaller form factors than those obtained using other methods and attributed this gap to the missing Coulomb-like corrections. The uncertainties in the form factors adopted in our work are considerably smaller than those of the other approaches.

The two amplitudes are treated at different perturbative orders: NLO (PB) and LO (WA). The NLO (WA) calculation of Ref. [45] for $B \to (\pi,K)\ell^+\ell^-$ demonstrates that one-loop annihilation corrections can introduce noticeable variations. However, in the current analysis, we use NLO (PB) + LO (WA) because the $B_c \to D^*\ell^+\ell^-$ NLO (WA) corrections are unavailable, which constitutes a limitation of our analysis. For final-state muons, we analyze the decay in both low- and high-q^2 regions, whereas for final-state tau leptons, only the high-q^2 region is kinematically allowed. To investigate NP signatures, we use the fitted values of NP Wilson coefficients (WCs) obtained from global-fit analyses of $b \to d$ transitions [46]. Furthermore, we present predictions for the physical observables over the allowed ranges of the NP WCs, as well as correlation plots between observables in both one-dimensional (1D) and two-dimensional (2D) NP scenarios.

The paper is organized as follows. In Section II, we present the formalism for analyzing the $B_c^+ \to D^{*+}\ell^+\ell^-$ decay, including the effective Hamiltonian and the decay amplitude. The hadronic matrix elements associated with the PB and WA amplitudes are parametrized in terms of transition form factors. Next, we give the four-fold angular distribution of the $B_c^+ \to D^{*+}(\to P_1P_2)\ell^+\ell^-$ decays, which contains the angular coefficients I_i. Finally, the section ends with the expressions for the helicity amplitudes, which contain the SM and NP WCs, as well as the transition form factors associated with both PB and WA amplitudes. In Section III, we present the formulae for the physical observables, followed by a phenomenological analysis of the $B_c^+ \to D^{*+}(\to P_1P_2)\ell^+\ell^-$ decays in both the SM and the selected 1D and 2D NP scenarios. Finally, in Section IV, we summarize the results of our study.

II. FORMALISM TO ANALYZE $B_c^+ \to D^{*+}\ell^+\ell^-$ DECAY

The semileptonic $B_c^+ \to D^{*+}\ell^+\ell^-$ decay receives contributions from the PB and WA topologies. In addition, it is affected by LD resonance effects, which primarily arise from intermediate vector-meson states that decay into a lepton pair. At the quark level, this decay is driven by the $b \to d\ell^+\ell^-$ transition, and its low-energy effective Hamiltonian can be written as [46, 47],

$$\mathcal{H}_{\rm eff} = -\frac{4G_F}{\sqrt{2}} V_{tb}V_{td}^* \left[\mathcal{H}_{\rm eff}^{(t)} + \lambda_u^{(d)}\mathcal{H}_{\rm eff}^{(u)}\right] + \text{h.c.}, \tag{1}$$

where G_F is the Fermi coupling constant, $V_{tb}V_{td}^*$ denotes the product of CKM matrix elements, and

$$\lambda_u^{(d)} = \frac{V_{ub}V_{ud}^*}{V_{tb}V_{td}^*}. \tag{2}$$

The forms of $\mathcal{H}_{\rm eff}^{(t)}$ and $\mathcal{H}_{\rm eff}^{(u)}$ in terms of the WCs C_i and the local quark operators O_i can be written as follows:

CPC Accepted

$$\mathcal{H}_{\rm eff}^{(t)} = C_1 O_1^c + C_2 O_2^c + \sum_{i=3}^{6} C_i O_i + \sum_{i=7,9,10} \left[(C_i + C_i^{NP}) O_i + C_i'^{NP} O_i' \right], \quad (3)$$

and

$$\mathcal{H}_{\rm eff}^{(u)} = C_1 (O_1^c - O_1^u) + C_2 (O_2^c - O_2^u). \quad (4)$$

It is important to note that the operator expressions in Eqs. (3) and (4) are taken from Refs. [48, 49], where they are written in the Chetyrkin–Misiak–Münz (CMM) basis, whereas the operators used for the WA amplitude in [42] are written in the BBL basis. Therefore, to maintain consistency with our PB amplitude, we use the following leading-order (LO) conversions between the CMM and BBL bases [50],

$$C_1{}^{BBL} = \frac{C_1{}^{CMM}}{2}, \quad C_2{}^{BBL} = C_2{}^{CMM} - \frac{C_1{}^{CMM}}{6}. \quad (5)$$

Using the effective Hamiltonian in Eq. (1), the PB amplitude for the decay is described as

$$\mathcal{M}^{PB}\left(B_c^+ \to D^{*+}\ell^+\ell^-\right) = \frac{G_F \alpha}{2\sqrt{2}\pi} V_{tb} V_{td}^* \left\{ T_\mu^{1,PB} (\bar{\ell}\gamma^\mu \ell) + T_\mu^{2,PB} (\bar{\ell}\gamma^\mu \gamma_5 \ell) \right\}, \quad (6)$$

where

$$T_\mu^{1,PB} = (C_9^{eff} + C_9^{NP}) \langle D^*(k,\epsilon)|\bar{d}\gamma_\mu(1-\gamma_5)b|B_c(p)\rangle + C_9'^{NP} \langle D^*(k,\epsilon)|\bar{d}\gamma_\mu(1+\gamma_5)b|B_c(p)\rangle - \frac{2m_b}{q^2}(C_7^{eff} + C_7^{NP}) \langle D^*(k,\epsilon)|\bar{d} i\sigma_{\mu\nu} q^\nu (1+\gamma_5) b|B_c(p)\rangle, \quad (7)$$

and

$$T_\mu^{2,PB} = (C_{10} + C_{10}^{NP}) \langle D^*(k,\epsilon)|\bar{d}\gamma_\mu(1-\gamma_5)b|B_c(p)\rangle + C_{10}'^{NP} \langle D^*(k,\epsilon)|\bar{d}\gamma_\mu(1+\gamma_5)b|B_c(p)\rangle. \quad (8)$$

The explicit forms of the effective WCs and local quark operators, including the LD resonance effects and NP contributions, are given in [40, 48–54] (see also Appendix A).

The hadronic matrix elements in Eqs. (7) and (8) are parametrized in terms of Lorentz-invariant form factors. The matrix elements for the vector and axial-vector quark currents are defined as

$$\langle D^*(k,\epsilon)|\bar{d}\gamma_\mu b|B_c(p)\rangle = \frac{2\epsilon_{\mu\nu\alpha\beta}}{m_{B_c} + m_{D^*}} \epsilon^{*\nu} p^\alpha k^\beta V(q^2), \quad (9)$$

$$\langle D^*(k,\epsilon)|\bar{d}\gamma_\mu\gamma_5 b|B_c(p)\rangle = i(m_{B_c} + m_{D^*}) g_{\mu\nu} \epsilon^{*\nu} A_1(q^2) - i\frac{P_\mu (\epsilon^* \cdot q)}{m_{B_c} + m_{D^*}} A_2(q^2) - i\frac{2m_{D^*}}{q^2} q_\mu (\epsilon^* \cdot q)[A_3(q^2) - A_0(q^2)], \quad (10)$$

where

$$A_3(q^2) = \frac{m_{B_c} + m_{D^*}}{2m_{D^*}} A_1(q^2) - \frac{m_{B_c} - m_{D^*}}{2m_{D^*}} A_2(q^2), \quad (11)$$

where $A_3(0) = A_0(0)$.

The tensor current matrix elements are written as

$$\langle D^*(k,\epsilon)|\bar{d} i\sigma_{\mu\nu} q^\nu b|B_c(p)\rangle = -2\epsilon_{\mu\nu\alpha\beta} \epsilon^{*\nu} p^\alpha k^\beta T_1(q^2), \quad (12)$$

$$\langle D^*(k,\epsilon)|\bar{d} i\sigma_{\mu\nu} q^\nu \gamma_5 b|B_c(p)\rangle = i\left[(m_{B_c}^2 - m_{D^*}^2) g_{\mu\nu} \epsilon^{*\nu} - (\epsilon^* \cdot q) P_\mu\right] T_2(q^2) + i(\epsilon^* \cdot q)\left[q_\mu - \frac{q^2}{m_{B_c}^2 - m_{D^*}^2} P_\mu\right] T_3(q^2). \quad (13)$$

In the naive factorization approach, the WA amplitude for the $B_c^+ \to D^{*+}\ell^+\ell^-$ decay is expressed as [42],

$$\mathcal{M}_{Ann} = V_{cb} V_{cd}^* \frac{i\alpha}{q^2} \frac{G_F}{2\sqrt{2}\pi} \left(\frac{C_1{}^{BBL}}{N_c} + C_2{}^{BBL} \right) \mathcal{T}_{ann}^\mu \bar{\ell}\gamma_\mu \ell, \quad (14)$$

where

$$\mathcal{T}_{ann}^\mu = \mathcal{T}_1^\mu + \mathcal{T}_2^\mu + \mathcal{T}_3^\mu + \mathcal{T}_4^\mu. \quad (15)$$

The explicit expressions for the hadronic matrix elements $\mathcal{T}_i^\mu$ are given in Ref. [42]. The corresponding WA form factors are computed within the BS framework [42, 55].

We emphasize that the WA form factors obtained from the BS calculation are, in general, complex-valued functions of q^2. For $X_{\rm ann} = T_{1\rm ann}, T_{2\rm ann}, T_{3\rm ann}, V_{\rm ann}$, we may write

$$X_{\rm ann}(q^2) = X_R(q^2) + iX_I(q^2) = |X_{\rm ann}(q^2)| e^{i\delta_X^{\rm WA}(q^2)}, \qquad \delta_X^{\rm WA}(q^2) = \arg X_{\rm ann}(q^2).$$

The imaginary parts arise from the pole structure of the BS integrals and represent absorptive contributions [42]. Therefore, the dynamical WA phase retained in our

CPC Accepted

calculation should be distinguished from the overall factor i/q^2 in Eq. (14), which by itself does not represent a dynamical strong phase. We retain both the real and imaginary parts of the BS WA form factors in the numerical analysis. In addition, rescattering strong phases from final-state interactions may contribute and are important for studies of CP-asymmetry observables [56, 57]. Because these effects are not included in our present calculations, CP-asymmetry observables are not considered in the main analysis of this work. Their possible impact should therefore be regarded as a residual hadronic systematic uncertainty in the PB–WA interference, particularly in the high-q^2 region.

A first estimate of the direct CP asymmetry for the differential branching ratio, together with its averaged values in the low- and high-q^2 bins, is presented in Appendix C.

In terms of form factors, the WA matrix elements can be parametrized as[1)]

$$\begin{aligned} T^{\mu}_{ann}(B_c \to D^*) = (m_{B_c} - m_{D^*})\Big[&T_{1ann} m^2_{B_c} \epsilon^{\mu} \\ &+ T_{2ann}(\epsilon\cdot q)p^{\mu} + T_{3ann}(\epsilon\cdot q)k^{\mu} \\ &+ \frac{i}{2} V_{ann}\epsilon^{\mu\nu\alpha\beta}\epsilon_{\nu}p_{\alpha}k_{\beta}\Big]. \end{aligned} \tag{16}$$

To analyze the physical observables, we adopt the four-fold differential decay distribution, which can be expressed in terms of the dilepton invariant mass squared, q^2, and the angular variables θ_ℓ, θ_V, and ϕ as [40, 48],

$$\begin{aligned} &\frac{d^4\Gamma}{dq^2\, d\cos\theta_\ell\, d\cos\theta_V\, d\phi} \\ &= \frac{9}{32\pi}\mathrm{Br}(D^* \to P_1P_2)\Big[I_{1s}\sin^2\theta_V + I_{1c}\cos^2\theta_V \\ &\quad + (I_{2s}\sin^2\theta_V + I_{2c}\cos^2\theta_V)\cos 2\theta_\ell \\ &\quad + (I_{6s}\sin^2\theta_V + I_{6c}\cos^2\theta_V)\cos\theta_\ell \\ &\quad + (I_3\cos 2\phi + I_9\sin 2\phi)\sin^2\theta_V\sin^2\theta_\ell \\ &\quad + (I_4\cos\phi + I_8\sin\phi)\sin 2\theta_V\sin 2\theta_\ell \\ &\quad + (I_5\cos\phi + I_7\sin\phi)\sin 2\theta_V\sin\theta_\ell\Big]. \end{aligned} \tag{17}$$

The expressions for the angular coefficients I_i in terms of the helicity amplitudes are the same as those used in previous analyses [40, 48] and are therefore not repeated here. Including the SM and NP WCs and the WA effects, the helicity amplitudes can be expressed as follows:

$$\begin{aligned} H^{1,D^*}_{\pm} =& -i(m^2_{B_c} - m^2_{D^*})\left[(C_9^{\rm eff} + C_9^{NP} - C_9^{\prime NP})\frac{A_1}{m_{B_c} - m_{D^*}} + \frac{2m_b}{q^2}(C_7^{\rm eff} + C_7^{NP})T_2\right] \\ &\pm i\sqrt{\lambda}\left[(C_9^{\rm eff} + C_9^{NP} + C_9^{\prime NP})\frac{V}{m_{B_c} + m_{D^*}} + \frac{2m_b}{q^2}(C_7^{\rm eff} + C_7^{NP})T_1\right] \\ &- iR_{PBAnn}\left[m^2_{B_c}(m_{B_c} - m_{D^*})T_{1\rm ann} \pm \tfrac{\sqrt{\lambda}}{2}(m_{B_c} - m_{D^*})V_{\rm ann}\right], \end{aligned} \tag{18}$$

$$H^{2,D^*}_{\pm} = -i(C_{10} + C_{10}^{NP} - C_{10}^{\prime NP})(m_{B_c} + m_{D^*})A_1 \pm i\sqrt{\lambda}(C_{10} + C_{10}^{NP} + C_{10}^{\prime NP})\frac{V}{m_{B_c} + m_{D^*}}, \tag{19}$$

$$\begin{aligned} H^{1,D^*}_{0} =& -\frac{i}{2m_{D^*}\sqrt{q^2}}\left[(C_9^{\rm eff} + C_9^{NP} - C_9^{\prime NP})\left((m^2_{B_c} - m^2_{D^*} - q^2)(m_{B_c} + m_{D^*})A_1 - \frac{\lambda}{m_{B_c} + m_{D^*}}A_2\right)\right. \\ &\left. + 2m_b(C_7^{\rm eff} + C_7^{NP})\left((m^2_{B_c} + 3m^2_{D^*} - q^2)T_2 - \frac{\lambda}{m^2_{B_c} - m^2_{D^*}}T_3\right)\right] \\ &- \frac{iR_{PBAnn}}{4\sqrt{q^2}m_{D^*}(m_{B_c} + m_{D^*})}(m^2_{D^*} - m^2_{B_c})\left[2m^2_{B_c}T_{1\rm ann}(q^2 - m^2_{B_c} + m^2_{D^*}) - \lambda(T_{2\rm ann} + T_{1\rm ann})\right], \end{aligned} \tag{20}$$

1) This expression is taken from [42], but the annihilation form factors are incorporated in our work according to the phase convention used in our previous work [49]. The effects of this choice appear in Eqs. (18)–(23) as an overall phase difference relative to [42], which does not affect the observables.

CPC Accepted

$$H_0^{2,D^*} = -\frac{i}{2m_{D^*}\sqrt{q^2}}(C_{10}+C_{10}^{NP}-C_{10}^{\prime NP}) \Big[(m_{B_c}^2-m_{D^*}^2-q^2)(m_{B_c}+m_{D^*})A_1 - \frac{\lambda}{m_{B_c}+m_{D^*}}A_2\Big], \tag{21}$$

$$H_t^{1,D^*} = -i\sqrt{\frac{\lambda}{q^2}}(C_9^{\rm eff}+C_9^{NP}-C_9^{\prime NP})A_0 - \frac{i\sqrt{\lambda}R_{PBAnn}}{4\sqrt{q^2}m_{D^*}}(m_{B_c}-m_{D^*})\Big[2m_{D^*}^2T_{1\rm ann}+(q^2+m_{B_c}^2-m_{D^*}^2)T_{2\rm ann}-(q^2-m_{B_c}^2+m_{D^*}^2)T_{3\rm ann}\Big], \tag{22}$$

$$H_t^{2,D^*} = -i\sqrt{\frac{\lambda}{q^2}}(C_{10}+C_{10}^{NP}-C_{10}^{\prime NP})A_0, \tag{23}$$

where

$$R_{PBAnn} = \left(\frac{V_{cb}V_{cd}^*}{V_{tb}V_{td}^*}\right)\left(\frac{C_1^{BBL}}{3}+C_2^{BBL}\right). \tag{24}$$

The relative weak phase between the PB and WA contributions is contained in the CKM ratio that appears in R_{PBAnn}. In the standard CKM phase convention, $V_{cb}V_{cd}^*$ is approximately real and negative, whereas $V_{tb}V_{td}^*$ carries the weak phase $+\beta$. Therefore, this CKM ratio determines the physically relevant relative weak phase.

$$\Delta\phi_{\rm WA-PB} = \arg\left(\frac{V_{cb}V_{cd}^*}{V_{tb}V_{td}^*}\right) \simeq \pi-\beta \simeq 158^\circ, \tag{25}$$

where $\beta \simeq 22^\circ$ is the CKM unitarity-triangle angle [58]. Correspondingly, $\cos\Delta\phi_{\rm WA-PB} \simeq -0.93$. This relative CKM phase is retained through the complex CKM ratio in R_{PBAnn} in all helicity amplitudes and therefore enters consistently in the PB–WA interference.

Since $\cos\Delta\phi_{\rm WA-PB} \simeq -0.93$, the CKM weak-phase difference strongly favors destructive PB–WA interference whenever the corresponding strong-phase cosine is positive. However, the complete interference pattern for observables is not determined by the weak phase alone, because the relative hadronic phase is q^2 dependent and can also differ among the helicity amplitudes. Therefore, the PB–WA interference need not remain universally destructive over the entire kinematic range. This phase structure is also relevant for the NP sensitivity, because the NP contributions modify the PB amplitude but do not introduce any new phase. Consequently, the NP plots are obtained in the presence of destructive PB(NP)–WA interference. However, our plots show that, although the PB NP sensitivity remains obscured by substantial destructive interference contributions, it is still achievable for the current 1σ and 2σ ranges of recent global fits of the PB NP WCs.

III. NUMERICAL INPUTS AND PHENOMENOLOGICAL ANALYSIS

In this section, we investigate the effects of NP through observables associated with $B_c^+ \to D^{*+}(\to P_1P_2)\ell^+\ell^-$ decays for $\ell = \mu, \tau$. The observables considered in this analysis are the differential branching fraction $d{\rm Br}/dq^2$, the lepton forward-backward asymmetry $A_{\rm FB}$, the longitudinal helicity fraction f_L, and the normalized angular coefficients $\langle I_i\rangle$. The expressions for these observables in terms of the angular coefficients I_i are as follows.

- Differential branching fraction:

$$\frac{d{\rm Br}(B_c^+ \to D^{*+}(\to P_1P_2)\ell^+\ell^-)}{dq^2} = \tau_{B_c}{\rm Br}(D^{*+}\to P_1P_2)\frac{(3I_{1c}+6I_{1s}-I_{2c}-2I_{2s})}{4}. \tag{26}$$

Neglecting the cascade decay $D^{*+} \to P_1P_2$,

$$\frac{d{\rm Br}(B_c^+ \to D^{*+}\ell^+\ell^-)}{dq^2} = \tau_{B_c}\frac{(3I_{1c}+6I_{1s}-I_{2c}-2I_{2s})}{4}. \tag{27}$$

- Lepton forward-backward asymmetry:

$$A_{\rm FB}(q^2) = \frac{6I_{6s}}{2(3I_{1c}+6I_{1s}-I_{2c}-2I_{2s})}. \tag{28}$$

- Longitudinal helicity fraction:

$$f_L(q^2) = \frac{3I_{1c}-I_{2c}}{3I_{1c}+6I_{1s}-I_{2c}-2I_{2s}}. \tag{29}$$

- Normalized angular coefficients:

$$\langle I_i\rangle = \frac{{\rm Br}(D^{*+}\to P_1P_2)\,I_i}{d\Gamma(B_c^+ \to D^{*+}(\to P_1P_2)\ell^+\ell^-)/dq^2}. \tag{30}$$

The required input parameters are listed in Table I. To determine the impact of NP, we consider several model-independent 1D and 2D NP scenarios involving the WCs C_7^{NP}, C_9^{NP}, C_{10}^{NP}, $C_9^{\prime NP}$, and $C_{10}^{\prime NP}$. The best-fit values and the corresponding 1σ and 2σ ranges of the NP WCs are taken from the global-fit analysis in [46]; their numerical values are summarized in Table II.

CPC Accepted

Table 1. Input parameters used in this study [59].

$m_{B_c} = 6.2749$ GeV	$m_\mu = 0.106$ GeV
$m_d = 0.0048$ GeV	$m_b = 4.18$ GeV
$m_\tau = 1.776$ GeV	$m_{D^*} = 2.010$ GeV
$\alpha^{-1} = 137$	$G_F = 1.166\times10^{-5}$ GeV^{-2}
$\lvert V_{tb}V_{td}^*\rvert = 8.1\times10^{-3}$	$\lvert V_{cb}\rvert = 0.041$
$\tau_{B_c} = 0.507\times10^{-12}$ sec	$\mathrm{Br}(D^{*+}\to D^0\pi^+) = 67.7\%$

Notably, the NP scenarios SI, SII, and SIII arise naturally in various simple NP models with tree-level leptoquark or Z' boson exchanges. Specifically, SI and SII can be generated in Z' models, whereas SIII can be realized through scalar or vector leptoquarks, as well as in a Z' model with purely left-handed couplings [60–62].

In the following subsections, we first discuss the predictions for the observables in different 1D NP scenarios and then extend our analysis to the 2D NP scenarios.

A. Probing NP signatures using 1D NP scenarios

In this subsection, we discuss the effects of the 1D NP scenarios SI–SIV on the differential branching fraction $d\mathrm{Br}/dq^2$, lepton FB asymmetry $A_{\rm FB}$, longitudinal helicity fraction f_L, and angular coefficients $\langle I_i\rangle$ for the decay $B_c^+\to D^{*+}\ell^+\ell^-$. The corresponding results are presented in Figs. 1–3. The plots are organized from left to right in three kinematic ranges: the low-q^2 muon range ($4m_\mu^2 \simeq 0.045\ \mathrm{GeV}^2 \le q^2 \le 8\ \mathrm{GeV}^2$), the high-$q^2$ muon range ($8 \le q^2 \le 18.18\ \mathrm{GeV}^2$), and the high-$q^2$ tau range ($14 \le q^2 \le 18.18\ \mathrm{GeV}^2$). The bands in these figures represent the uncertainties in the predicted observables, arising mainly from the uncertainties in the form factors. To enhance discrimination among different NP scenarios, the color bands are plotted using the lower 1σ limit for SI–SIII and the upper 1σ limit for SIV, as given in Table II. The scenarios are color-coded as follows:

- SI (C_9^{NP}): red,
- SII (C_{10}^{NP}): green,
- SIII ($C_9^{NP} = -C_{10}^{NP}$): blue,
- SIV ($C_9^{NP} = -C_{10}^{NP} = -C_9^{\prime NP} = -C_{10}^{\prime NP}$): orange.

The left panel in the first row of Fig. 1 shows the differential branching fraction $d\mathrm{Br}/dq^2$. In the low-q^2 muon range, SI (red band) enhances the branching fraction relative to the SM prediction (gray band). The SIII and SIV scenarios remain close to the SM prediction, whereas SII suppresses the branching fraction.

In the middle panel of the first row, we show the predictions for $d\mathrm{Br}/dq^2$ in the remaining range $8 \le q^2 \le q^2_{\rm max}$, including the charmonium resonance region. In the high-q^2 muon range, the NP predictions tend to lie below the SM prediction across much of the kinematic range, with substantial overlap among the NP scenarios. Therefore, the high-q^2 differential branching fraction is sensitive to NP effects, but this substantial overlap limits the ability to distinguish among different NP scenarios. For the case of τ as the final-state lepton, shown in the rightmost panel of the first row, the branching fraction decreases with increasing q^2. The hierarchy among the NP scenarios differs from that in the muon case because of the significant impact of lepton-mass effects in the helicity amplitudes. Among the considered scenarios, SI exhibits the largest deviation from the SM prediction, whereas SII shows the least pronounced deviation relative to the SM over most of the allowed kinematic range.

The second row of Fig. 1 displays the forward-backward asymmetry $A_{\rm FB}$. In the low-q^2 muon range, all scenarios predict positive values of $A_{\rm FB}$ over a sizable part of the kinematic range. The shift in the zero crossing of $A_{\rm FB}$ depends on the NP scenario. From the trend shown in Fig. 1, the zero crossing of $A_{\rm FB}$ in the SM occurs approximately at $q^2 \simeq 6.75\ \mathrm{GeV}^2$, while the SII, SIII, and SIV scenarios exhibit zero crossings near $q^2 \simeq 6.73\ \mathrm{GeV}^2$, $7.61\ \mathrm{GeV}^2$, and $7.19\ \mathrm{GeV}^2$, respectively. However, the SI scenario remains positive throughout the low-q^2 interval.

In the high q^2 muon range, we also incorporate the effects of the LD resonance, as well as the interference

Table 2. Best-fit values and corresponding 1σ and 2σ ranges for the NP WCs in different 1D and 2D NP scenarios [46].

Scenario	Fit Parameters	Best Fit	1σ	2σ	$\chi^2_{H_i,min}$	Pull$_{H_i}$	p-value(%)
SI	C_9^{NP}	−1.37	[−2.97, −0.47]	[−7.65, 0.26]	1.23	1.63	94
SII	C_{10}^{NP}	0.96	[0.31, 1.74]	[−0.27, 2.88]	1.55	1.53	90
SIII	$C_9^{NP} = -C_{10}^{NP}$	−0.54	[−0.90, −0.20]	[−1.29, 0.13]	1.32	1.60	93
SIV	$C_9^{NP} = -C_{10}^{NP} = -C_9^{\prime NP} = -C_{10}^{\prime NP}$	−0.58	[−1.06, −0.20]	[−4.04, 0.12]	1.28	1.61	93
SV	(C_7^{NP}, C_9^{NP})	(0.11, −1.55)	([−0.05, 0.34], [−3.05, −0.61])	([−0.18, 1.46], [−10.07, 0.18])	0.77	1.25	94
SVI	$(C_9^{NP}, C_9^{\prime NP})$	(−2.22, 1.18)	([−6.55, −0.63], [−2.99, 2.89])	([−7.58, 0.23], [−3.92, 3.81])	0.87	1.22	92
SVII	$(C_9^{NP}, C_{10}^{\prime NP})$	(−1.83, −0.38)	([−6.58, −0.6], [−1.2, 0.32])	([−7.6, 0.25], [−1.8, 0.99])	0.95	1.20	91
SVIII	$(C_9^{NP} = -C_9^{\prime NP}, C_{10}^{NP} = +C_{10}^{\prime NP})$	(−1.73, 0.44)	([−3.34, −0.19], [0.04, 0.95])	([−4.1, 0.51], [−0.34, 4.52])	0.88	1.22	92

CPC Accepted

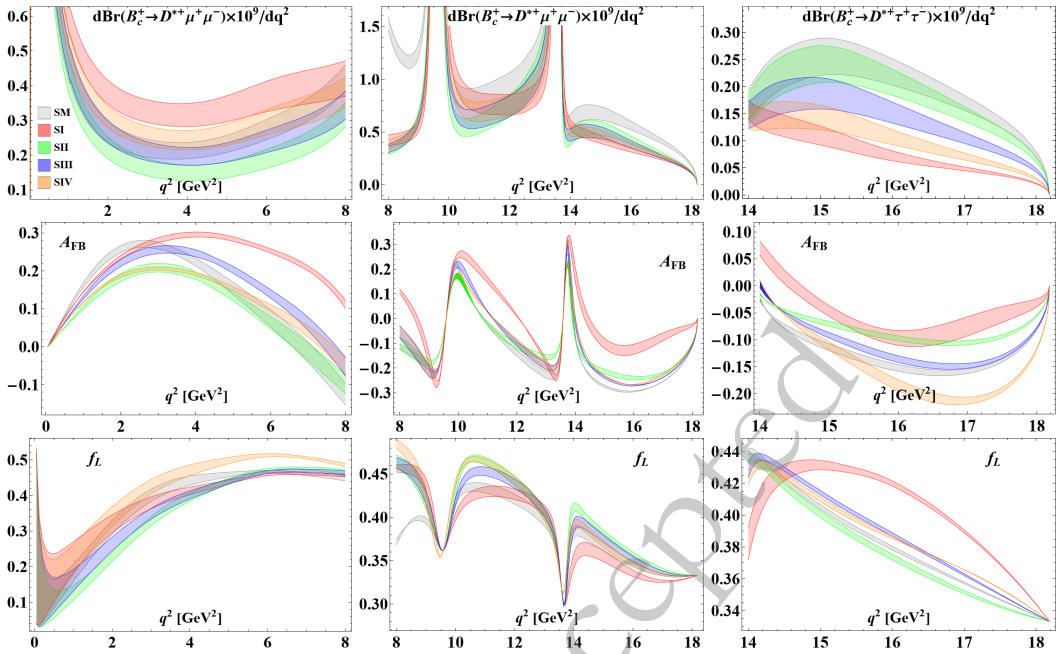

Fig. 1. Predictions for the differential branching fraction $d\mathrm{Br}/dq^2$, the forward-backward asymmetry A_{FB}, and the longitudinal helicity fraction f_L for the decay $B_c^+ \to D^{*+}\ell^+\ell^-$ in the SM and the 1D NP scenarios SI–SIV. The first and second columns show these observables (from top to bottom) as functions of the dilepton invariant mass squared q^2 for the low- and high-q^2 ranges of the muon channel, respectively. The third column shows the corresponding predictions for the high-q^2 range of the tau channel.

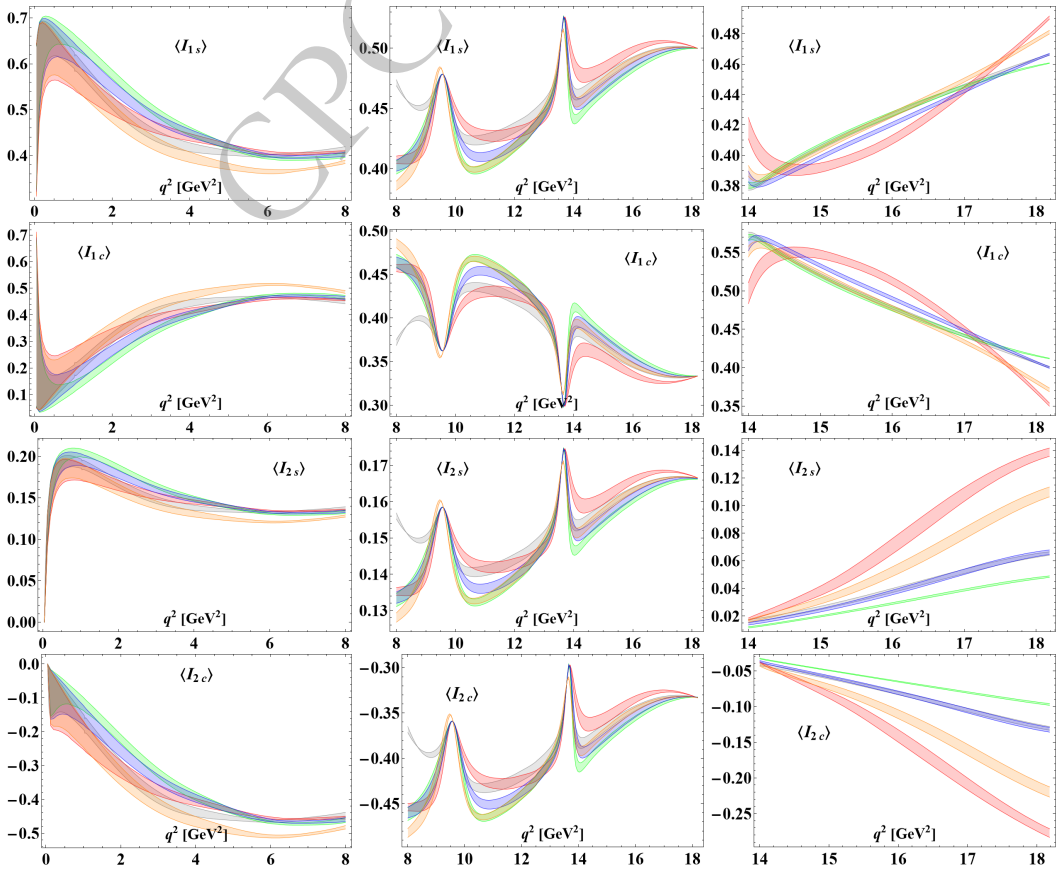

Fig. 2. Predictions of the normalized angular coefficients $\langle I_{1s}\rangle$, $\langle I_{1c}\rangle$, $\langle I_{2s}\rangle$, and $\langle I_{2c}\rangle$ for the decay $B_c^+ \to D^{*+}\ell^+\ell^-$ in the SM and the 1D NP scenarios SI–SIV. The panel arrangement is the same as in Fig. 1.

CPC Accepted

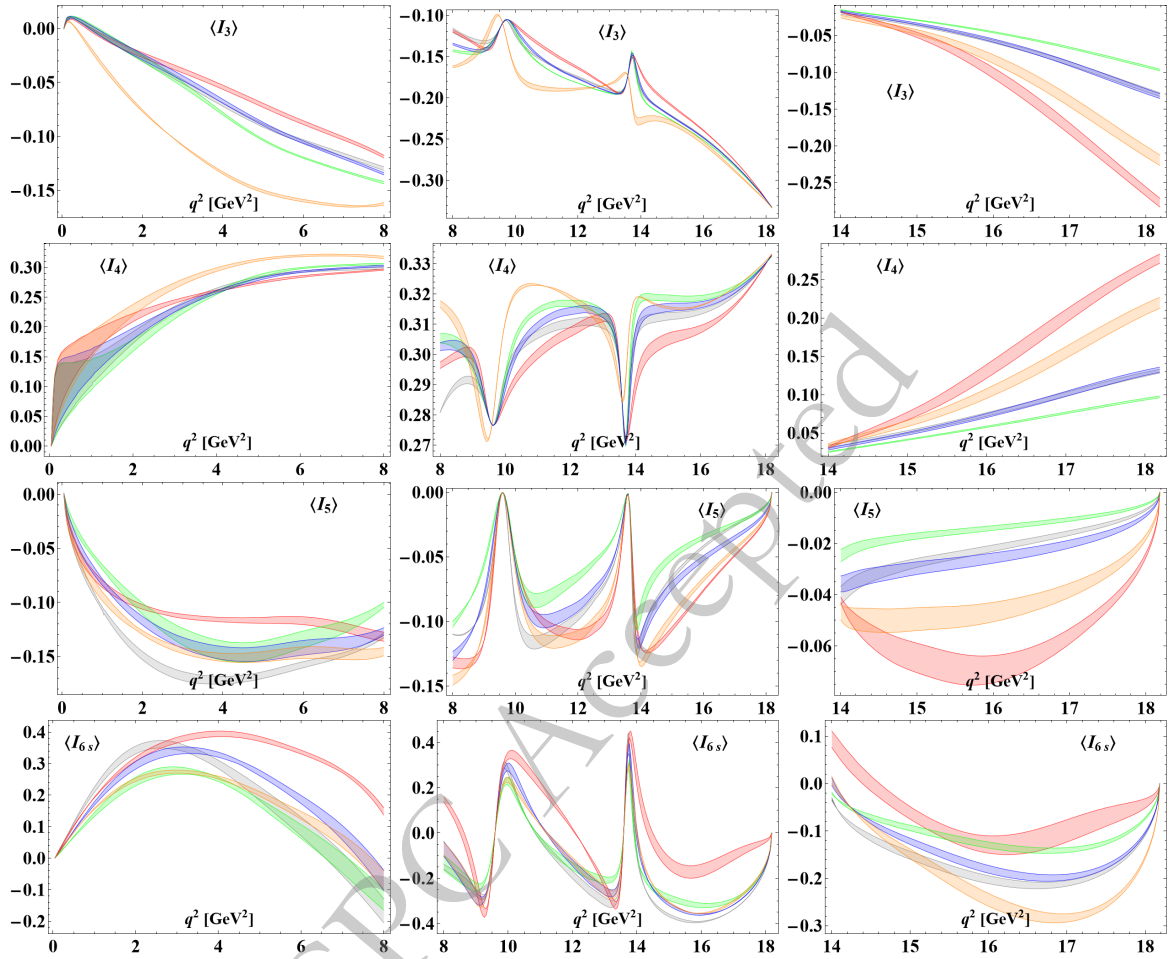

CPC Accepted

Fig. 3. Predictions for the normalized angular coefficients $\langle I_3\rangle$, $\langle I_4\rangle$, $\langle I_5\rangle$, and $\langle I_{6s}\rangle$ in the decay $B_c^+ \to D^{*+}\ell^+\ell^-$ within the SM and the 1D NP scenarios SI–SIV. The panel arrangement is the same as in Fig. 1.

between the WA and PB amplitudes. The SI scenario exhibits a notable deviation over the plotted range, while the other scenarios show small deviations and partially overlap with one another. For τ as the final-state lepton, $A_{\rm FB}$ is distinguishable for all the NP scenarios under consideration relative to the SM prediction. However, scenarios SII, SIII, and SIV approximately overlap with the SM at $14 \le q^2 \le 15$ GeV^2. Additionally, scenario SI shows a clear departure from the SM across the whole kinematic range for the τ, and it is clearly distinguishable from the other NP scenarios.

The longitudinal helicity fraction f_L versus q^2 is shown in the third row of Fig. 1. In the low-q^2 range for muons, f_L increases with increasing q^2 for all the considered 1D NP scenarios. At the lowest value of q^2, the NP bands remain close to one another. The SIV scenario becomes distinguishable around $q^2 \approx 5$ GeV^2, while the other scenarios remain closer to the SM prediction. In the high-q^2 range for the muon, f_L shows sharp variations around the charmonium resonance ranges. Between the resonances, the SII and SIII scenarios tend to increase f_L, while SI yields relatively smaller values. Above the $\psi(2S)$ range, all predictions decrease and gradually converge near the endpoint. Thus, f_L provides moderate separation among the considered NP scenarios.

For the τ lepton, f_L as a function of q^2 is shown in the far-right panel of the third row of Fig. 1. The figure shows that, among all the NP scenarios under consideration, scenario SI starts with the lowest value of f_L. After crossing all the other NP scenarios and the SM at $q^2 \approx 14.3$ GeV^2, it produces the most pronounced enhancement of f_L and shows a clear distinction from the other NP scenarios. In contrast to SI, SIII, and SIV, scenario SII predicts lower values of the longitudinal helicity fraction than the SM predictions over most of the allowed kinematic range.

Overall, the 1D NP scenarios produce visible deviations from the SM results in these observables. From Fig. 1, in the low-q^2 muon range, the differential branching fraction and A_{FB} show the largest visible separation among the NP bands, whereas f_L exhibits comparatively greater overlap among the scenarios. Therefore, in the

low-q^2 muon range, $d\mathrm{Br}/dq^2$ and A_{FB} are expected to be more suitable observables for distinguishing the 1D NP scenarios, whereas f_L is less suitable. However, for the τ lepton, all three observables are sensitive to significant NP deviations from the SM predictions in the allowed kinematic range.

The predictions for the normalized angular coefficients $\langle I_{1s}\rangle$, $\langle I_{1c}\rangle$, $\langle I_{2s}\rangle$, and $\langle I_{2c}\rangle$ in the SM and the 1D NP scenarios are presented in Fig. 2, while the corresponding results for $\langle I_3\rangle$, $\langle I_4\rangle$, $\langle I_5\rangle$, and $\langle I_{6s}\rangle$ are shown in Fig. 3. The plots are arranged in the same order as discussed previously. For the angular coefficients $\langle I_{1s}\rangle$ and $\langle I_{2s}\rangle$, all NP scenarios exhibit relatively similar behavior in the low-q^2 region, with the SII scenario generally predicting slightly larger values than the other scenarios. In the high-q^2 muon region, visible deviations among the scenarios emerge near the resonance regions, where interference between the weak annihilation and PB amplitudes becomes significant. For the τ channel, the spread among the NP scenarios increases considerably with increasing q^2, particularly for the SI and SIV scenarios.

The coefficients $\langle I_{1c}\rangle$ and $\langle I_{2c}\rangle$ exhibit a stronger dependence on the NP WCs. In the low-q^2 muon region, the SII and SIV scenarios lead to comparatively larger deviations from the SM prediction, whereas the SI and SIII scenarios remain relatively closer to the SM values. For the τ channel, the differences among the NP scenarios become more pronounced at higher q^2 values. This effect is especially visible in $\langle I_{2c}\rangle$, which becomes more negative in the SI and SIV scenarios than in the SM prediction.

The observables $\langle I_3\rangle$ and $\langle I_4\rangle$ also show visible sensitivity to the NP scenarios. The coefficient $\langle I_3\rangle$ exhibits the largest deviations in the SI and SIV scenarios, particularly when the τ lepton is considered in the final state. In contrast, $\langle I_4\rangle$ in the low-q^2 muon region increases steadily with q^2 and shows moderate deviations across the NP scenarios. In the high-q^2 muon region, the NP scenarios are relatively distinguishable, whereas for the τ lepton case, all NP scenarios are distinct for $q^2 \geq 15$ GeV^2 and can be clearly discriminated from one another.

For the angular coefficient $\langle I_5\rangle$, we find that, for the μ lepton in the low-q^2 range, the NP scenarios can be distinguished from the SM predictions. However, some scenarios, such as SII, SIII, and SIV, overlap with each other in the kinematic range $q^2 \approx 2-7$ GeV^2. In contrast, scenario SI overlaps with the others only for $q^2 \leq 2.5$ GeV^2 and $q^2 \geq 6.5$ GeV^2. In the high-q^2 μ range, the angular coefficient $\langle I_5\rangle$ is strongly affected by the charmonium resonances, whereas the NP bands show visible separation away from these regions. For the τ final state, the hierarchy among the scenarios becomes clearer: SI gives the largest magnitude in the negative direction, SII gives the smallest, and SIII and SIV lie in between.

The coefficient $\langle I_{6s}\rangle$ shows strong sensitivity to the NP WCs. This behavior is expected because, in the convention used in Eq. (28), I_{6s} enters directly in the numerator of the forward-backward asymmetry. Thus, $\langle I_{6s}\rangle$ follows the main trends observed in A_{FB} and provides complementary information on the helicity structure of the decay.

In the high-q^2 range, its behavior is also shaped by the resonance contribution and by the interference between WA and PB amplitudes.

Overall, the angular coefficients exhibit substantial sensitivity to the NP WCs and provide complementary information to the branching fraction, forward-backward asymmetry, and longitudinal helicity fraction. In particular, the observables $\langle I_{2c}\rangle$, $\langle I_5\rangle$, and $\langle I_{6s}\rangle$ appear to be especially sensitive to the interplay between the weak annihilation amplitudes and the NP-modified short-distance contributions. These effects become more pronounced in the τ channel because of the enhanced lepton-mass dependence of the helicity amplitudes.

In Fig. 4, we present the binned predictions of the observables for the 1D NP scenarios using bar plots, in which the complete prediction ranges associated with the NP WCs and form factor uncertainties are displayed. For each observable, the results are given for three different bins. The kinematic ranges for the low-q^2 μ bin and the high-q^2 τ bin are the same as before, whereas for the high-q^2 μ bin, we choose the range $[14, q^2_{\mathrm{max}}]$ GeV^2. In each bin, the gray horizontal band represents the SM prediction together with its theoretical uncertainty, which originates mainly from the uncertainties in the form factors. The colored bars correspond to the different 1D NP scenarios and display the full allowed prediction ranges obtained by varying the NP WCs within their corresponding 1σ (lighter shade) and 2σ (darker shade) intervals. Furthermore, each set of bars contains three individual predictions corresponding to the allowed NP WC ranges with lower, central, and upper fixed values of the form factors, thereby incorporating both the hadronic uncertainties and the allowed NP parameter space simultaneously. The previous color convention for the NP scenarios is maintained throughout the analysis. Therefore, the bar plots provide a compact representation of the possible deviations that each NP scenario can generate, with its 1σ and 2σ ranges, for a given observable within the selected kinematic bins.

A general feature observed in these plots is that the low-q^2 range has comparatively larger SM uncertainty bands owing to its enhanced sensitivity to hadronic effects and weak annihilation contributions. In contrast, the high-q^2 ranges exhibit smaller SM uncertainties but comparatively larger relative deviations induced by the NP scenarios. After excluding the charmonium-dominated range, the high-q^2 μ bin $[14, q^2_{\mathrm{max}}]$ GeV^2 provides a comparatively cleaner region for studying NP effects. However, the full kinematic interval $8 \leq q^2 \leq 18.18$ GeV^2 includes resonance structures and is therefore also af-

Accepted

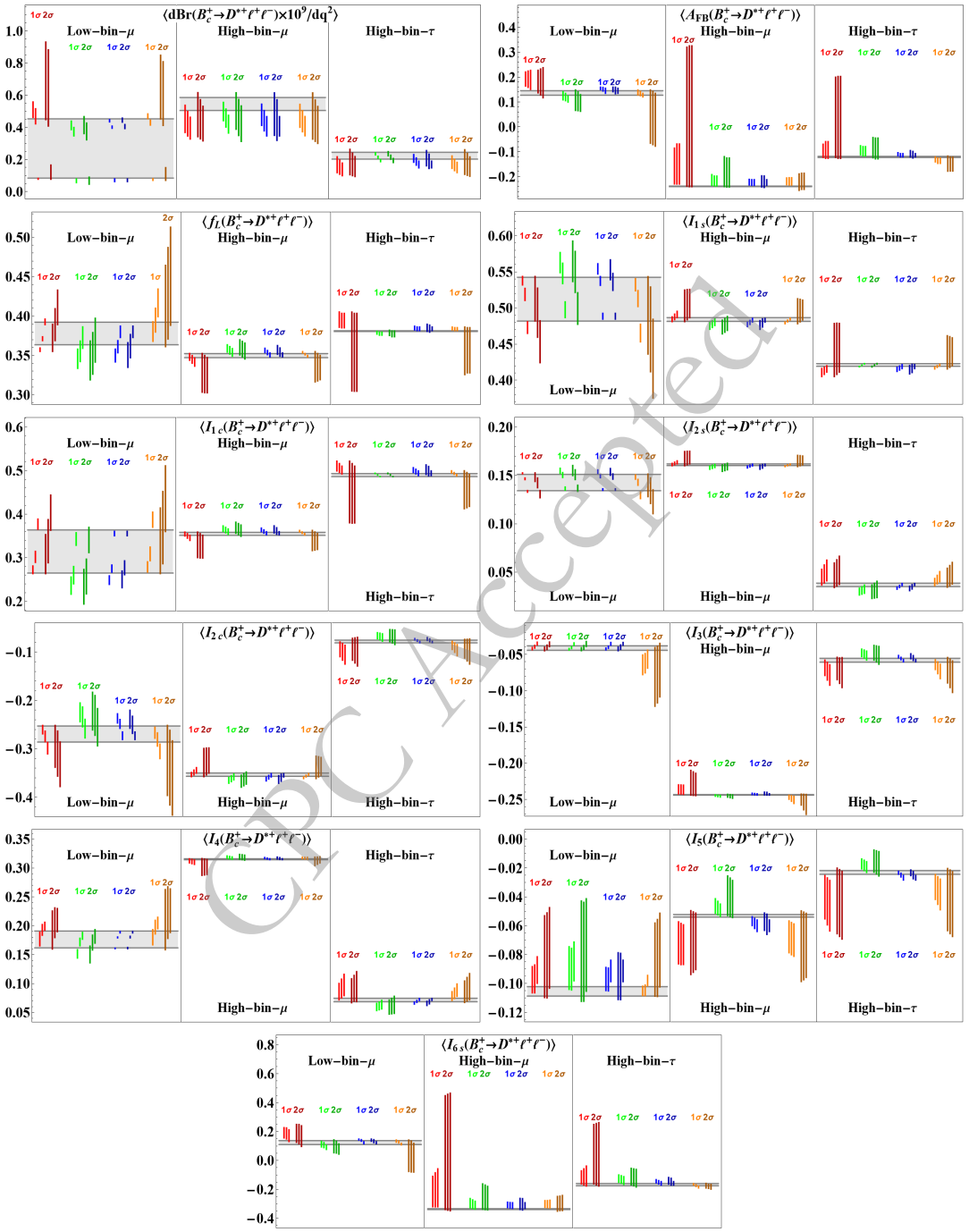

CPC Accepted

Fig. 4. Binned predictions for the observables in the 1D NP scenarios SI–SIV are shown. For each observable, results are presented in the low-q^2 muon bin ($[0.045, 8]\,\mathrm{GeV}^2$), the high-$q^2$ resonance-free muon bin ($[14, 18.18]\,\mathrm{GeV}^2$), and the high-$q^2$ tau bin ($[14, 18.18]\,\mathrm{GeV}^2$). The colored bars indicate the allowed 1σ and 2σ ranges of the NP WCs, including form-factor uncertainties, whereas the horizontal gray bands represent the SM predictions.

fected by LD resonance contributions and WA interference. Among the considered scenarios, SI and SIV generally produce the largest deviations from the SM predictions for most observables. We note that the uncertainty bands shown in the present analysis do not include an independent uncertainty associated with possible additional WA rescattering phases beyond those already encoded in the complex BS form factors. Consequently, the PB–WA interference in the high-q^2 region carries a residual hadronic phase uncertainty that is not quantified separately in the present work. In particular, sizable shifts are visible in the differential branching ratio, the FB asym-

metry, and the angular coefficients. The SII and SIII scenarios, on the other hand, tend to remain comparatively closer to the SM predictions for several observables, although noticeable deviations are still present in specific bins.

An important phenomenological implication of these results is that some observables show partially separated prediction ranges among the different NP scenarios, especially in the high-q^2 τ range. Although sizable overlap remains once the WC ranges and form-factor uncertainties are included, this behavior suggests that future precision measurements of these observables at LHCb or other high-luminosity flavor experiments could help discriminate among the different NP scenarios and constrain the underlying WCs associated with the $b \to d\ell^+\ell^-$ transition. The combined possible minimum and maximum predictions obtained from any of the full 1σ and 2σ ranges of the NP WCs are summarized in Table III.

The correlation plots shown in Fig. 5 illustrate the interplay between the integrated branching fraction and the observables $\langle A_{\rm FB}\rangle$ and $\langle f_L\rangle$ for different 1D NP scenarios in the low bin for the muon channel and in the high bin for the tau channel. In the muon channel, the correlation between $\langle A_{\rm FB}\rangle$ and $\mathrm{Br}(B_c^+ \to D^{*+}\mu^+\mu^-)$ shows a clear sep-

Table 3. Minimum and maximum values of the observables in the SM and in the 1D scenarios SI, SII, SIII, and SIV. The three bins correspond, respectively, to the low-q^2 muon range ($[0.045, 8]\ \mathrm{GeV}^2$), the high-$q^2$ muon range ($[14, 18.18]\ \mathrm{GeV}^2$), and the high-$q^2$ tau-lepton range ($[14, 18.18]\ \mathrm{GeV}^2$).

Observable	range	SM	SI	SII	SIII	SIV
	Low-q^2 (μ)	(0.083, 0.452)	(0.077, 0.930)	(0.046, 0.465)	(0.062, 0.456)	(0.070, 0.847)
$\mathrm{Br}\times 10^9$	High-q^2 (μ)	(0.484, 0.568)	(0.289, 0.598)	(0.286, 0.598)	(0.293, 0.597)	(0.273, 0.596)
	High-q^2 (τ)	(0.171, 0.216)	(0.060, 0.234)	(0.150, 0.219)	(0.112, 0.226)	(0.062, 0.231)
	Low-q^2 (μ)	(0.127, 0.145)	(0.117, 0.237)	(0.062, 0.147)	(0.133, 0.158)	(−0.077, 0.147)
$A_{\rm FB}$	High-q^2 (μ)	(−0.240, −0.238)	(−0.240, 0.325)	(−0.241, −0.120)	(−0.243, −0.197)	(−0.255, −0.187)
	High-q^2 (τ)	(−0.123, −0.118)	(−0.126, 0.202)	(−0.128, −0.043)	(−0.125, −0.096)	(−0.178, −0.117)
	Low-q^2 (μ)	(0.363, 0.392)	(0.355, 0.432)	(0.319, 0.397)	(0.335, 0.387)	(0.361, 0.512)
f_L	High-q^2 (μ)	(0.347, 0.352)	(0.302, 0.352)	(0.345, 0.369)	(0.348, 0.362)	(0.316, 0.354)
	High-q^2 (τ)	(0.380, 0.381)	(0.304, 0.404)	(0.373, 0.381)	(0.379, 0.389)	(0.325, 0.385)
	Low-q^2 (μ)	(0.481, 0.542)	(0.424, 0.543)	(0.477, 0.592)	(0.484, 0.566)	(0.375, 0.543)
$\langle I_{1s}\rangle$	High-q^2 (μ)	(0.481, 0.486)	(0.481, 0.525)	(0.464, 0.488)	(0.470, 0.485)	(0.478, 0.512)
	High-q^2 (τ)	(0.419, 0.422)	(0.405, 0.478)	(0.418, 0.422)	(0.408, 0.421)	(0.415, 0.461)
	Low-q^2 (μ)	(0.264, 0.363)	(0.263, 0.443)	(0.193, 0.369)	(0.231, 0.360)	(0.263, 0.510)
$\langle I_{1c}\rangle$	High-q^2 (μ)	(0.351, 0.358)	(0.299, 0.358)	(0.349, 0.381)	(0.352, 0.372)	(0.316, 0.362)
	High-q^2 (τ)	(0.486, 0.493)	(0.379, 0.521)	(0.486, 0.493)	(0.488, 0.512)	(0.412, 0.499)
	Low-q^2 (μ)	(0.134, 0.150)	(0.126, 0.152)	(0.133, 0.160)	(0.134, 0.156)	(0.110, 0.151)
$\langle I_{2s}\rangle$	High-q^2 (μ)	(0.160, 0.161)	(0.160, 0.174)	(0.154, 0.162)	(0.156, 0.161)	(0.159, 0.170)
	High-q^2 (τ)	(0.034, 0.038)	(0.034, 0.066)	(0.022, 0.040)	(0.030, 0.038)	(0.034, 0.059)
	Low-q^2 (μ)	(−0.285, −0.252)	(−0.377, −0.251)	(−0.293, −0.183)	(−0.280, −0.220)	(−0.436, −0.251)
$\langle I_{2c}\rangle$	High-q^2 (μ)	(−0.356, −0.350)	(−0.357, −0.298)	(−0.379, −0.348)	(−0.371, −0.351)	(−0.361, −0.315)
	High-q^2 (τ)	(−0.080, −0.075)	(−0.128, −0.069)	(−0.084, −0.053)	(−0.080, −0.070)	(−0.124, −0.073)
	Low-q^2 (μ)	(−0.044, −0.038)	(−0.044, −0.032)	(−0.044, −0.032)	(−0.044, −0.033)	(−0.121, −0.034)
$\langle I_3\rangle$	High-q^2 (μ)	(−0.244, −0.243)	(−0.244, −0.210)	(−0.248, −0.243)	(−0.243, −0.240)	(−0.270, −0.242)
	High-q^2 (τ)	(−0.060, −0.055)	(−0.095, −0.054)	(−0.063, −0.037)	(−0.060, −0.049)	(−0.102, −0.054)

Continued on next page

CPC Accepted

Table 3-continued from previous page

Observable	range	SM	SI	SII	SIII	SIV
$\langle I_4 \rangle$	Low-q^2 (μ)	(0.161, 0.190)	(0.159, 0.230)	(0.136, 0.193)	(0.160, 0.189)	(0.158, 0.267)
	High-q^2 (μ)	(0.314, 0.315)	(0.287, 0.316)	(0.313, 0.323)	(0.314, 0.318)	(0.304, 0.319)
	High-q^2 (τ)	(0.068, 0.074)	(0.066, 0.120)	(0.047, 0.077)	(0.062, 0.073)	(0.067, 0.116)
$\langle I_5 \rangle$	Low-q^2 (μ)	(−0.108, −0.102)	(−0.110, −0.047)	(−0.112, −0.041)	(−0.111, −0.078)	(−0.108, −0.051)
	High-q^2 (μ)	(−0.054, −0.052)	(−0.093, −0.049)	(−0.054, −0.025)	(−0.065, −0.051)	(−0.098, −0.049)
	High-q^2 (τ)	(−0.024, −0.021)	(−0.069, −0.020)	(−0.025, −0.007)	(−0.028, −0.021)	(−0.067, −0.020)
$\langle I_{6s} \rangle$	Low-q^2 (μ)	(0.109, 0.136)	(0.097, 0.248)	(0.044, 0.141)	(0.115, 0.147)	(−0.080, 0.140)
	High-q^2 (μ)	(−0.340, −0.334)	(−0.347, 0.464)	(−0.341, −0.164)	(−0.342, −0.263)	(−0.350, −0.243)
	High-q^2 (τ)	(−0.175, −0.160)	(−0.176, 0.260)	(−0.183, −0.055)	(−0.170, −0.119)	(−0.198, −0.159)

CPC Accepted

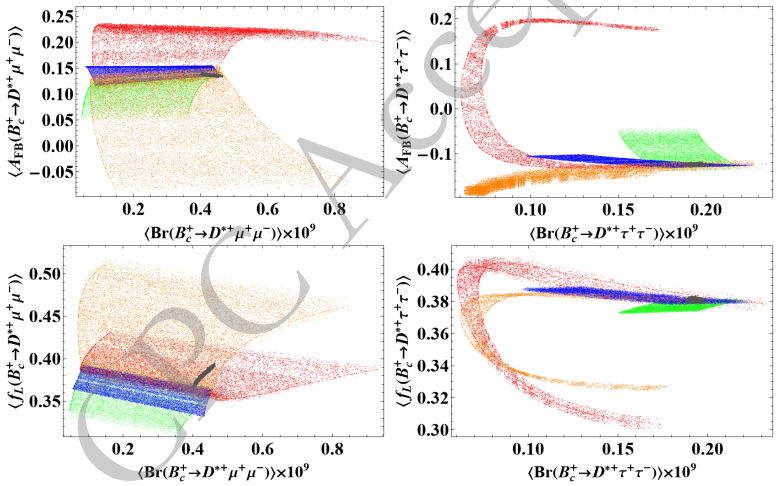

Fig. 5. Correlations between the integrated branching fraction and the observables $\langle A_{\rm FB} \rangle$ and $\langle f_L \rangle$ in the 1D NP scenarios SI–SIV. The left panels correspond to the low-q^2 bin for the muon channel, whereas the right panels show the high-q^2 bin for the tau channel. The spread of points reflects the form factor uncertainties and the WC uncertainties within the 2σ range.

aration among the NP scenarios. The SI scenario predicts the largest positive values of $\langle A_{\rm FB} \rangle$, together with an enhanced branching fraction, whereas SII yields comparatively smaller asymmetry values. The SIII and SIV scenarios remain closer to the SM-like range, with noticeable overlap. For the τ channel, the SIV scenario produces the most negative values, which increase with increasing branching ratio, whereas SI exhibits the widest spread in the allowed range, lying mostly in the positive range. In the SII scenario, the allowed points show an anticorrelation between the integrated branching fraction and $\langle A_{FB} \rangle$, such that larger branching-fraction values are associated with smaller values of $\langle A_{FB} \rangle$.

The lower panels display the correlations involving the longitudinal helicity fraction $\langle f_L \rangle$. In the muon mode, a positive correlation is observed for the NP scenarios, with larger branching fractions corresponding to larger values of $\langle f_L \rangle$. The SI and SIV scenarios allow comparatively larger longitudinal polarization. In the τ channel, the allowed ranges for SII and SIII become more compressed because of the restricted phase space. The observable $\langle f_L \rangle$ remains relatively large throughout the kinematic range in the SI and SIV scenarios, indicating enhanced longitudinal polarization contributions in the heavy-lepton case. Overall, the correlation plots demonstrate that combined measurements of the branching fraction, $\langle A_{\rm FB} \rangle$, and $\langle f_L \rangle$ can provide useful discrimination among different NP scenarios. The τ channel is found to be particularly sensitive to NP effects.

B. Probing NP signatures using 2D NP Scenarios

We now discuss the effects of the 2D NP scenarios SV–SVIII on the observables associated with the decay $B_c^+ \to D^{*+}\ell^+\ell^-$. The corresponding predictions for the differential branching fraction $d{\rm Br}/dq^2$, the forward-back-

ward asymmetry $A_{\rm FB}$, and the longitudinal helicity fraction f_L are shown in Fig. 6. To distinguish among the different NP scenarios, the color bands are plotted using the left-side 1σ values for SV–SVII and the right-side 1σ value for SVIII.

The color coding of the 2D scenarios is as follows:

- SV (C_7^{NP}, C_9^{NP}): red,
- SVI (C_9^{NP}, $C_9'^{NP}$): green,
- SVII (C_9^{NP}, $C_{10}'^{NP}$): blue,
- SVIII ($C_9^{NP} = -C_9'^{NP}$, $C_{10}^{NP} = +C_{10}'^{NP}$): orange.

The top row of Fig. 6 presents the differential branching fraction. In the low-q^2 range for the muon channel, all 2D NP scenarios tend to enhance the branching fraction relative to the SM prediction, with the SVII scenario producing the largest enhancement over most of the kinematic range. The SVI scenario predicts values comparatively closer to the SM prediction, while the SV and SVIII scenarios lie between these two cases. In the high-q^2 range for the muon channel, the branching fraction exhibits pronounced sensitivity to the NP WCs near the resonance regions. The SVII scenario again shows the largest enhancement, whereas the SVI scenario remains comparatively suppressed. For the τ channel, the hierarchy among the NP scenarios changes significantly. The SVII and SVIII scenarios predict comparatively smaller branching fractions than the SM band at higher q^2, while the SV scenario yields the smallest values over most of the allowed range.

The second row of Fig. 6 displays the forward-backward asymmetry $A_{\rm FB}$. In the low-q^2 range for the muon channel, the SVII scenario produces the largest positive asymmetry, while the SVI scenario predicts a rapid decrease toward negative values near the upper end of the low-q^2 range. The SV and SVIII scenarios also remain distinct and do not exhibit a zero crossing of $A_{\rm FB}$ in this range. In the high-q^2 range for the muon channel, all scenarios exhibit sizable distortions around the resonance regions due to the interplay between weak annihilation and PB amplitudes. The SVII scenario produces the largest positive enhancement, whereas the SVI scenario generates large negative deviations at higher q^2 values. For the τ mode, the differences among the NP scenarios become particularly pronounced. The SVII scenario predicts positive values of $A_{\rm FB}$ over most of the kinematic range, while the SVI scenario develops large negative values. The SV and SVIII scenarios are distinguishable from the SM band but exhibit similar behavior.

The third row of Fig. 6 shows the longitudinal helicity fraction f_L. In the low-q^2 muon range, all scenarios predict an increase with q^2, with the SVI and SVIII scenarios yielding larger values. The spread among the scenarios remains moderate compared with those for the

CPC Accepted

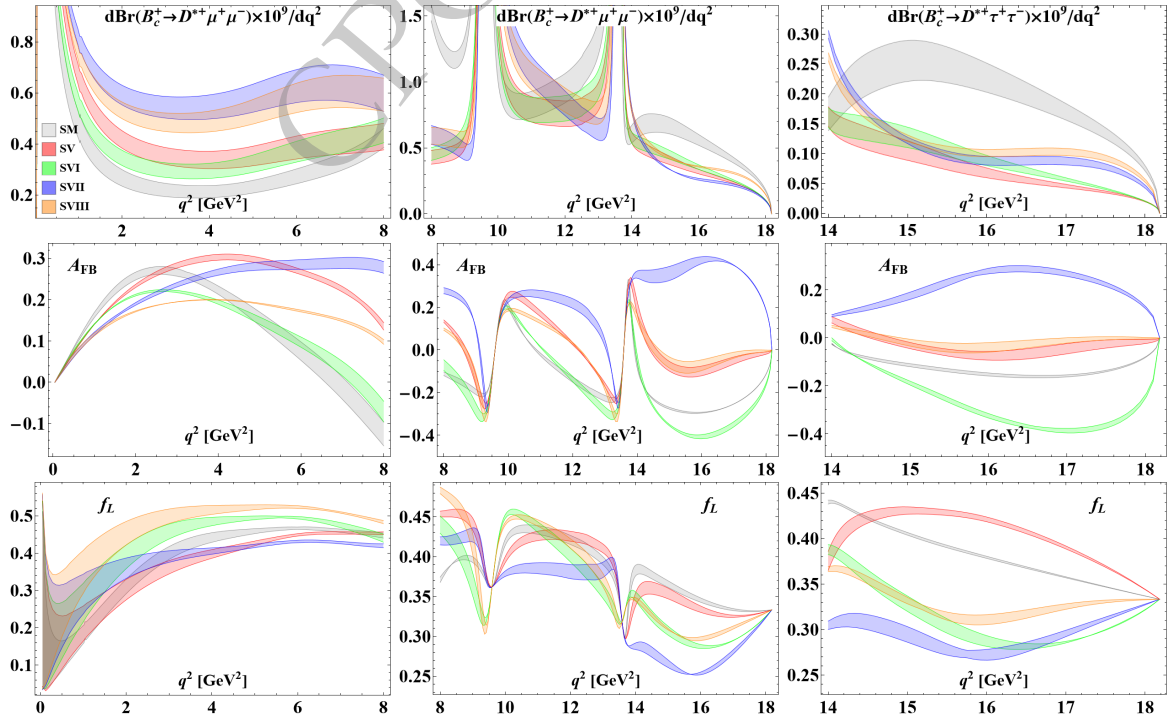

Fig. 6. Predictions for the differential branching fraction $d{\rm Br}/dq^2$, the forward–backward asymmetry $A_{\rm FB}$, and the longitudinal helicity fraction f_L for the decay $B_c^+ \to D^{*+}\ell^+\ell^-$ within the SM and the two-dimensional (2D) NP scenarios SV–SVIII. The first and second columns show these observables (from top to bottom) as functions of the dilepton invariant mass squared q^2 in the low- and high-q^2 ranges of the muon channel, respectively. The third column shows the corresponding predictions for the high-q^2 range of the tau channel.

branching fraction and forward-backward asymmetry. In the high-q^2 muon range, noticeable deviations appear near the resonance regions, with the SVII scenario predicting comparatively smaller values of f_L at larger q^2. For the τ channel, the SV scenario gives the largest longitudinal polarization fraction, whereas the SVII scenario predicts the smallest values over most of the allowed kinematic range. The SVI and SVIII scenarios also predict distinctly lower values of f_L compared with the SM band.

The predictions for the normalized angular coefficients $\langle I_{1s}\rangle$, $\langle I_{1c}\rangle$, $\langle I_{2s}\rangle$, and $\langle I_{2c}\rangle$ for the 2D NP scenarios are shown in Fig. 7, while the corresponding results for $\langle I_3\rangle$, $\langle I_4\rangle$, $\langle I_5\rangle$, and $\langle I_{6s}\rangle$ are displayed in Fig. 8. The figures are arranged in the same order as before. The angular coefficients $\langle I_{1s}\rangle$ and $\langle I_{2s}\rangle$ show moderate sensitivity to the NP WCs in the low-q^2 muon range. The SVII scenario generally produces the largest enhancement above $q^2 \approx 5$ GeV^2, whereas the SVIII scenario predicts comparatively smaller values. In the high-q^2 muon range, the spread among the NP scenarios becomes more apparent near the resonance regions. For the τ channel, both $\langle I_{1s}\rangle$ and $\langle I_{2s}\rangle$ exhibit a substantial spread among the NP scenarios at higher q^2 values. The coefficients $\langle I_{1c}\rangle$ and $\langle I_{2c}\rangle$ display a comparatively stronger dependence on the NP scenarios. In the low-q^2 range, the SVIII scenario generally produces larger deviations from the SM prediction, whereas the SV and SVII scenarios remain relatively close to the SM values. For the τ, the hierarchy among the NP scenarios changes significantly. For $\langle I_{1c}\rangle$, scenarios SVI–SVIII show substantial deviations from the SM predictions over most of the allowed kinematic range, whereas scenario SV deviates less from the SM and yields predictions opposite to those of SVI–SVIII in the interval $15 \le q^2 \le 17$ GeV^2. For $\langle I_{2c}\rangle$, SV shows the most pronounced deviations, whereas scenario SVII yields predictions opposite to those of SV, SVI, and SVIII.

The observables $\langle I_3\rangle$ and $\langle I_4\rangle$, presented in Fig. 8, also show sensitivity to the NP WCs. In the low-q^2 muon range, $\langle I_3\rangle$ is more suitable than $\langle I_4\rangle$ because it is relatively more sensitive to the NP scenarios. For the τ mode, however, both $\langle I_3\rangle$ and $\langle I_4\rangle$ are comparably good observables, as they exhibit decreasing and increasing values,

CPC Accepted

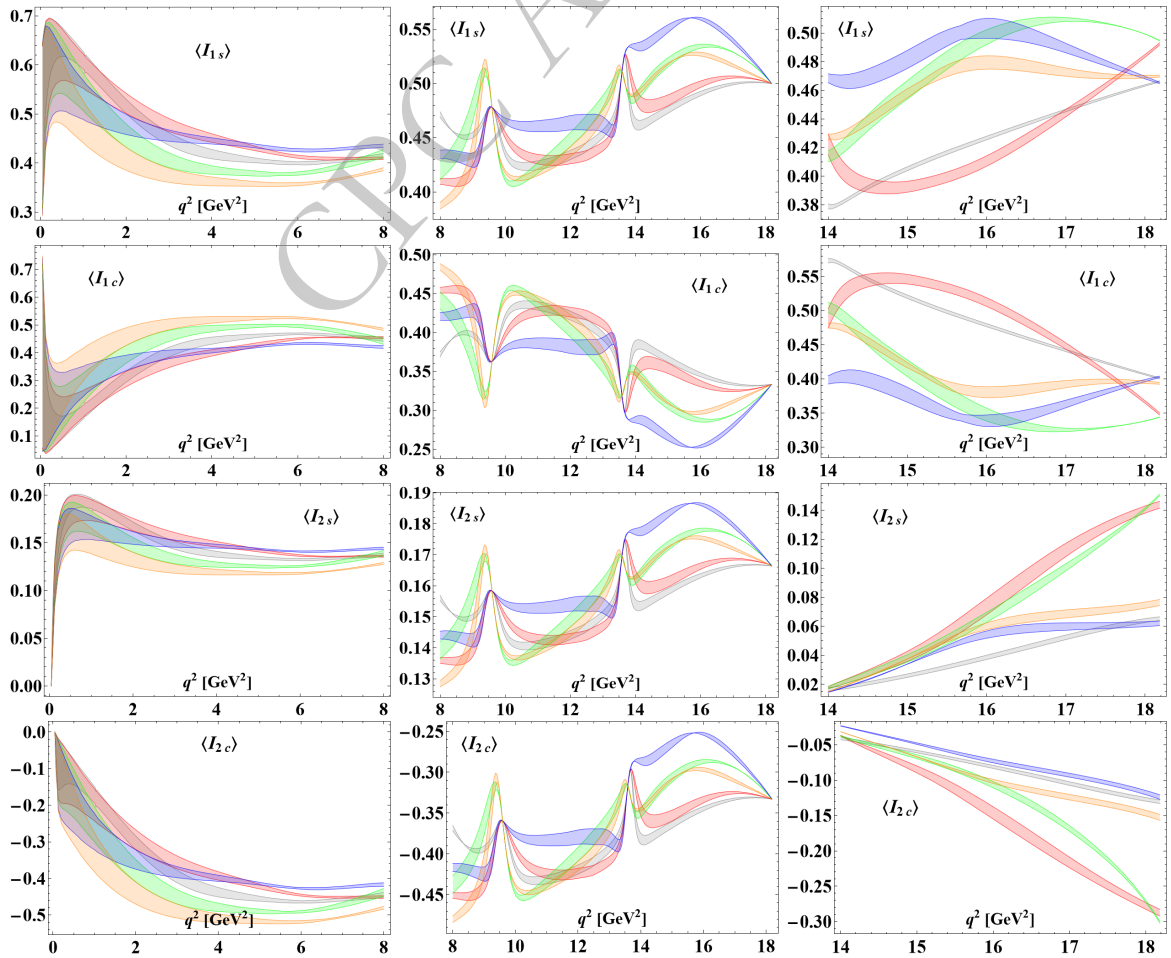

Fig. 7. Predictions for the normalized angular coefficients $\langle I_{1s}\rangle$, $\langle I_{1c}\rangle$, $\langle I_{2s}\rangle$, and $\langle I_{2c}\rangle$ in the decay $B_c^+ \to D^{**}\ell^+\ell^-$ within the SM and the 2D NP scenarios SV–SVIII. The panel arrangement is the same as in Fig. 6.

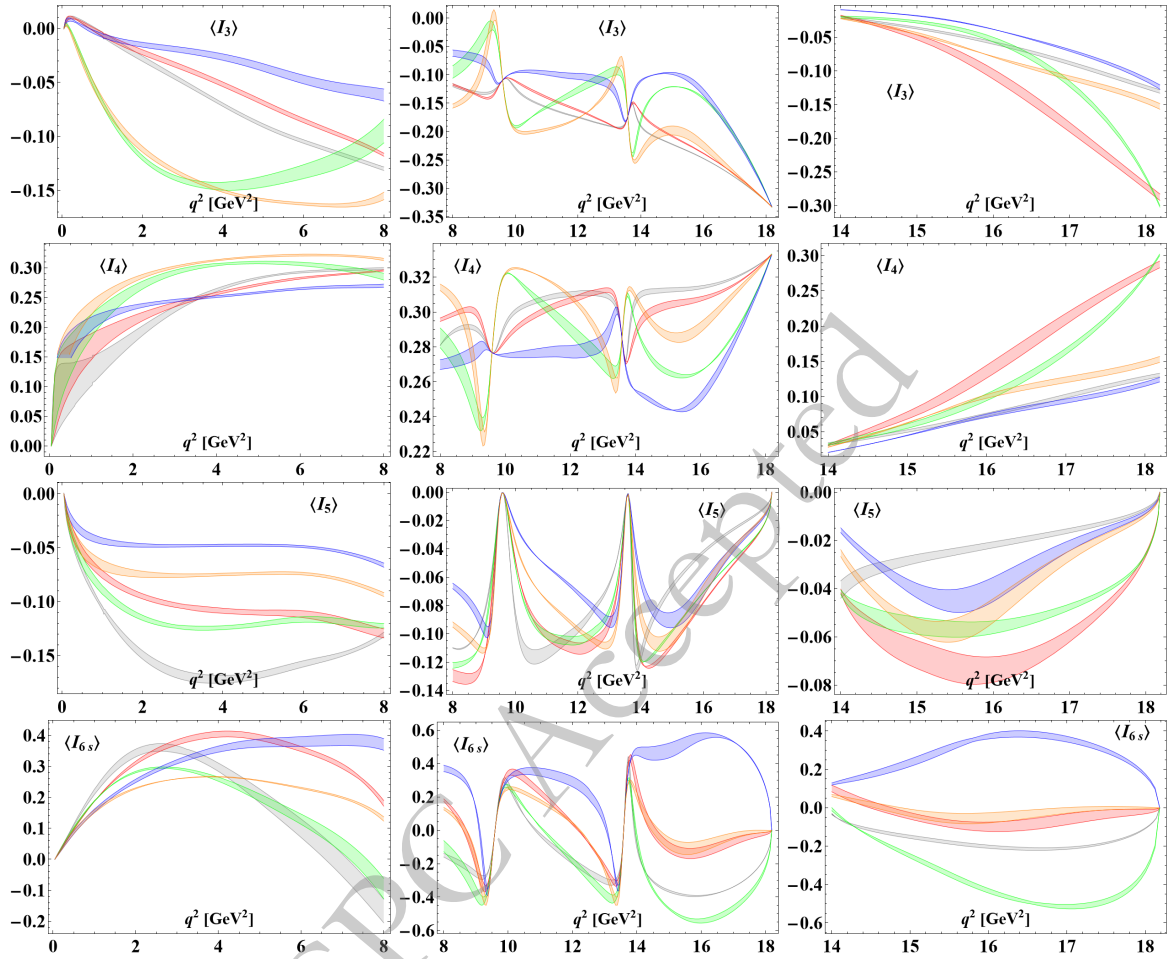

CPC Accepted

Fig. 8. Predictions for the normalized angular coefficients $\langle I_3\rangle$, $\langle I_4\rangle$, $\langle I_5\rangle$, and $\langle I_{6s}\rangle$ of the decay $B_c^+ \to D^{*+}\ell^+\ell^-$ in the SM and in the two-dimensional NP scenarios SV–SVIII. The panels are arranged as in Fig. 6.

respectively, for all NP scenarios with nearly equivalent magnitudes. The largest deviations from the SM case are observed for scenarios SV and SVI. For the coefficient $\langle I_5\rangle$, all 2D NP scenarios yield negative values over most of the kinematic range. In the low-q^2 muon range, $\langle I_5\rangle$ shows a clear dependence on the NP WCs. Scenario SVII yields the least negative values and deviates substantially from the SM predictions. Notably, all NP scenarios clearly deviate from the SM results and can be discriminated from one another. In the high-q^2 muon range, the observable is strongly affected by the charmonium resonance structures. Therefore, the sharp variations in this range may not be interpreted as purely NP effects. For the high-q^2 τ channel, the hierarchy changes: SV yields the largest negative magnitude, SVII remains closer to the SM band, and SVI and SVIII lie between them. Thus, $\langle I_5\rangle$ is one of the suitable observables for exploring the 2D NP scenarios.

The angular coefficient $\langle I_{6s}\rangle$ exhibits one of the strongest sensitivities to the 2D NP scenarios. In the low-q^2 muon range, all scenarios except SVI produce sizable positive values, whereas in the high-q^2 range the observable develops large deviations. In particular, the SVI scenario generates substantial negative deviations in the τ channel, while the SVII scenario predicts comparatively large positive values over most of the allowed kinematic range. In summary, the

angular observables in the 2D NP scenarios exhibit richer phenomenological behavior than those in the corresponding 1D scenarios because of the simultaneous variation of two NP WCs. Several observables, especially $\langle I_{1c}\rangle$, $\langle I_{2c}\rangle$, $\langle I_3\rangle$, $\langle I_5\rangle$, and $\langle I_{6s}\rangle$, show substantial sensitivity to the interference between the weak annihilation amplitudes and the NP-modified short-distance contributions. These effects become particularly pronounced in the τ channel, making these observables promising probes for distinguishing different NP scenarios in future experimental studies.

Figure 9 shows the binned predictions for the observables in the 2D NP scenarios SV–SVIII. The results are presented for three different bins, as discussed previously for Fig. 4. The gray horizontal bands represent the SM

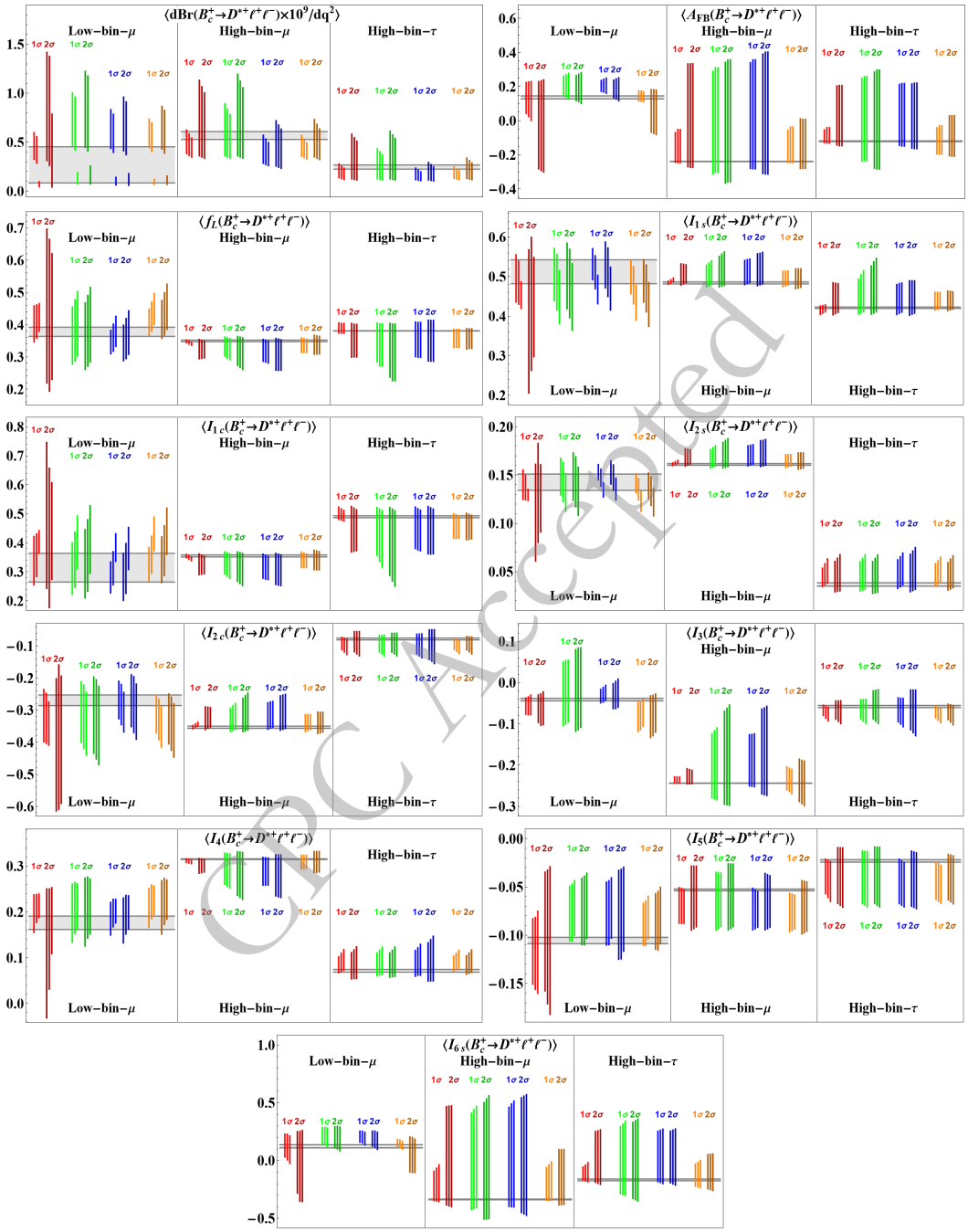

CPC Accepted

Fig. 9. Binned predictions for the observables in $B_c^+ \to D^{**}\ell^+\ell^-$ in the SM and the two-dimensional NP scenarios SV–SVIII. The panels show the low-q^2 muon bin ($[0.045, 8]\,\mathrm{GeV}^2$), the high-$q^2$ resonance-free muon bin ($[14, 18.18]\,\mathrm{GeV}^2$), and the high-$q^2$ tau bin ($[14, 18.18]\,\mathrm{GeV}^2$). The colored bars indicate the allowed 1σ and 2σ NP ranges, including form-factor uncertainties, whereas the gray bands denote the corresponding SM predictions.

predictions together with their theoretical uncertainties, while the colored bars correspond to the predictions of the different 2D NP scenarios. As before, the lighter and darker shades indicate the 1σ and 2σ ranges of the NP WCs, respectively. Each set of bars illustrates the effects of the allowed NP parameter space for the lower, central, and upper values of the form factors. Thus, the bar plots provide a compact illustration of the possible deviations generated by the 2D NP scenarios in different observables for the three bins. Compared with the corresponding 1D scenarios, the 2D scenarios generally produce wider prediction ranges because of the simultaneous variation of two NP WCs. The largest deviations are observed in both the low- and high-q^2 ranges, where the SM

uncertainties are comparatively smaller and the sensitivity to NP effects becomes more pronounced. The τ channel continues to display enhanced sensitivity to NP effects because of the sizable lepton-mass contributions entering the helicity amplitudes. However, when the complete 1σ and 2σ ranges of the NP WCs are considered, overlap of the NP predictions with the SM band and with one another appears to be inevitable.

From a phenomenological perspective, the 2D NP scenarios yield broader predictions than the corresponding 1D cases. The simultaneous modification of two WCs enhances the correlations among the observables and allows sizable departures from the SM predictions, even in observables that remain comparatively stable in the 1D scenarios. Consequently, a combined analysis of multiple observables in different kinematic ranges may provide strong constraints on the allowed NP parameter space in future experimental measurements. The combined possible minimum and maximum predictions corresponding to any of the full 1σ and 2σ ranges of the NP WCs are summarized in Table IV.

The correlation plots for the 2D NP scenarios, shown in Fig. 10, exhibit richer phenomenology because two NP WCs are varied simultaneously. The upper panels display the correlation between the integrated branching fraction and $\langle A_{\rm FB}\rangle$ for different 2D NP scenarios in the low bin for the muon channel and in the high bin for the tau channel. In the muon channel, the allowed ranges show sizable spreads, particularly for the red scenario, which extends to both large positive and negative values of $\langle A_{\rm FB}\rangle$. The green and blue scenarios predominantly populate the positive-asymmetry region and remain comparatively more constrained. The orange scenario occupies an intermediate range, with moderate deviations from the SM-like values. In the τ channel, the allowed parameter space becomes more compressed along the branching-fraction axis, while $\langle A_{\rm FB}\rangle$ develops both positive and negative branches. The green scenario shows the largest spread, whereas the blue scenario remains comparatively narrow and concentrated around moderate asymmetry values.

Similarly, the lower panels of Fig. 10 display the correlations involving the longitudinal helicity fraction $\langle f_L\rangle$ for the low-bin muon and high-bin tau modes. In the muon mode, the red scenario produces the broadest allowed range and extends toward significantly larger values of $\langle f_L\rangle$, while the green and blue scenarios favor comparatively smaller longitudinal polarization fractions. The orange scenario remains localized in the intermediate range. For the τ channel, the blue and green scenarios exhibit the widest spread in $\langle f_L\rangle$, with the former and latter extending toward comparatively lower and higher values of the branching fraction, respectively.

The correlation plots for the 2D NP scenarios show that the simultaneous variation of two NP WCs produces broader allowed ranges of the observables than in the corresponding 1D scenarios. The correlation between the integrated branching fraction and $\langle A_{FB}\rangle$ is especially useful, since different 2D scenarios populate different regions of parameter space in both the μ and τ channels. The correlations involving $\langle f_L\rangle$ are comparatively more compressed, but they still provide a complementary check on the decay. Although the allowed ranges of different scenarios partially overlap, the combined use of the branching fraction, $\langle A_{FB}\rangle$, and $\langle f_L\rangle$ can help distinguish among the 2D NP scenarios and constrain the WCs associated with the $b \to d\,\ell^+\ell^-$ transition in future precision measurements.

IV. CONCLUSIONS

We have investigated the FCNC semileptonic decay $B_c^+ \to D^{*+}\ell^+\ell^-$, with $\ell = \mu, \tau$, within a model-independent

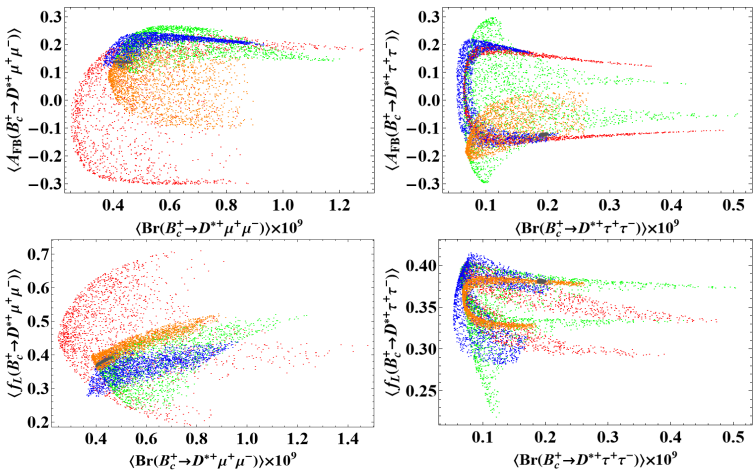

Fig. 10. Correlation plots between the integrated branching fraction and the observables $\langle A_{\rm FB}\rangle$ and $\langle f_L\rangle$ for $B_c^+ \to D^{*+}\ell^+\ell^-$, obtained from the allowed parameter space of the 2D NP scenarios SV–SVIII. The correlations are shown for the low-q^2 bin in the muon channel and the high-q^2 bin in the tau channel. The spread of points includes form-factor and WC uncertainties within the 2σ range.

CPC Accepted

Table 4. Minimum and maximum values of the observables in the SM and in the two-dimensional scenarios SV, SVI, SVII, and SVIII. The three bins correspond, respectively, to the low-q^2 muon range ($[0.045, 8]\ \mathrm{GeV}^2$), the high-$q^2$ muon range ($[14, 18.18]\ \mathrm{GeV}^2$), and the high-$q^2$ tau-lepton range ($[14, 18.18]\ \mathrm{GeV}^2$).

Observable	range	SM	SV	SVI	SVII	SVIII
	Low-q^2 (μ)	(0.083, 0.452)	(0.042, 1.417)	(0.074, 1.232)	(0.059, 0.957)	(0.068, 0.861)
$\mathrm{Br}\times 10^9$	High-q^2 (μ)	(0.484, 0.568)	(0.287, 1.079)	(0.287, 1.171)	(0.181, 0.686)	(0.273, 0.689)
	High-q^2 (τ)	(0.171, 0.216)	(0.059, 0.534)	(0.059, 0.591)	(0.047, 0.242)	(0.062, 0.286)
	Low-q^2 (μ)	(0.127, 0.145)	(−0.300, 0.238)	(0.101, 0.280)	(0.116, 0.251)	(−0.081, 0.181)
A_{FB}	High-q^2 (μ)	(−0.240, −0.238)	(−0.274, 0.332)	(−0.365, 0.355)	(−0.313, 0.401)	(−0.280, 0.009)
	High-q^2 (τ)	(−0.123, −0.118)	(−0.147, 0.205)	(−0.283, 0.295)	(−0.164, 0.219)	(−0.208, 0.028)
	Low-q^2 (μ)	(0.363, 0.392)	(0.194, 0.695)	(0.261, 0.514)	(0.288, 0.442)	(0.358, 0.525)
f_L	High-q^2 (μ)	(0.347, 0.352)	(0.294, 0.353)	(0.261, 0.363)	(0.258, 0.357)	(0.308, 0.366)
	High-q^2 (τ)	(0.380, 0.381)	(0.299, 0.403)	(0.226, 0.404)	(0.287, 0.413)	(0.324, 0.387)
	Low-q^2 (μ)	(0.481, 0.542)	(0.206, 0.611)	(0.370, 0.580)	(0.416, 0.585)	(0.369, 0.543)
$\langle I_{1s}\rangle$	High-q^2 (μ)	(0.481, 0.486)	(0.479, 0.531)	(0.473, 0.564)	(0.477, 0.560)	(0.469, 0.519)
	High-q^2 (τ)	(0.419, 0.422)	(0.402, 0.484)	(0.404, 0.543)	(0.402, 0.489)	(0.414, 0.463)
	Low-q^2 (μ)	(0.264, 0.363)	(0.169, 0.744)	(0.205, 0.510)	(0.204, 0.451)	(0.263, 0.518)
$\langle I_{1c}\rangle$	High-q^2 (μ)	(0.351, 0.358)	(0.290, 0.361)	(0.250, 0.368)	(0.252, 0.363)	(0.307, 0.374)
	High-q^2 (τ)	(0.486, 0.493)	(0.368, 0.523)	(0.263, 0.521)	(0.361, 0.524)	(0.410, 0.501)
	Low-q^2 (μ)	(0.134, 0.150)	(0.062, 0.178)	(0.108, 0.171)	(0.124, 0.164)	(0.108, 0.151)
$\langle I_{2s}\rangle$	High-q^2 (μ)	(0.160, 0.161)	(0.159, 0.176)	(0.157, 0.186)	(0.158, 0.186)	(0.156, 0.172)
	High-q^2 (τ)	(0.034, 0.038)	(0.029, 0.067)	(0.027, 0.067)	(0.029, 0.074)	(0.030, 0.066)
	Low-q^2 (μ)	(−0.285, −0.252)	(−0.614, −0.156)	(−0.466, −0.196)	(−0.388, −0.189)	(−0.446, −0.250)
$\langle I_{2c}\rangle$	High-q^2 (μ)	(−0.356, −0.350)	(−0.359, −0.289)	(−0.366, −0.252)	(−0.362, −0.250)	(−0.372, −0.306)
	High-q^2 (τ)	(−0.080, −0.075)	(−0.130, −0.055)	(−0.130, −0.060)	(−0.153, −0.050)	(−0.124, −0.070)
	Low-q^2 (μ)	(−0.044, −0.038)	(−0.103, −0.022)	(−0.118, 0.085)	(−0.063, 0.007)	(−0.132, −0.029)
$\langle I_3\rangle$	High-q^2 (μ)	(−0.244, −0.243)	(−0.244, −0.208)	(−0.297, −0.049)	(−0.272, −0.064)	(−0.297, −0.186)
	High-q^2 (τ)	(−0.060, −0.055)	(−0.099, −0.044)	(−0.098, −0.019)	(−0.127, −0.018)	(−0.102, −0.052)
	Low-q^2 (μ)	(0.161, 0.190)	(−0.030, 0.253)	(0.125, 0.275)	(0.132, 0.235)	(0.152, 0.272)
$\langle I_4\rangle$	High-q^2 (μ)	(0.314, 0.315)	(0.284, 0.316)	(0.229, 0.331)	(0.231, 0.324)	(0.286, 0.331)
	High-q^2 (τ)	(0.068, 0.074)	(0.053, 0.123)	(0.057, 0.122)	(0.049, 0.145)	(0.064, 0.116)
	Low-q^2 (μ)	(−0.108, −0.102)	(−0.181, −0.029)	(−0.109, −0.035)	(−0.123, −0.029)	(−0.115, −0.050)
$\langle I_5\rangle$	High-q^2 (μ)	(−0.054, −0.052)	(−0.094, −0.026)	(−0.094, −0.027)	(−0.094, −0.036)	(−0.098, −0.043)
	High-q^2 (τ)	(−0.024, −0.021)	(−0.070, −0.009)	(−0.070, −0.008)	(−0.072, −0.012)	(−0.067, −0.016)
	Low-q^2 (μ)	(0.109, 0.136)	(−0.355, 0.258)	(0.082, 0.294)	(0.095, 0.253)	(−0.108, 0.201)
$\langle I_{6s}\rangle$	High-q^2 (μ)	(−0.340, −0.334)	(−0.400, 0.472)	(−0.503, 0.570)	(−0.473, 0.570)	(−0.382, 0.113)
	High-q^2 (τ)	(−0.175, −0.160)	(−0.206, 0.264)	(−0.351, 0.361)	(−0.213, 0.272)	(−0.259, 0.051)

CPC Accepted

NP framework for the underlying $b \to d\ell^+\ell^-$ transition. The analysis includes the PB contribution, LD resonance effects, and the WA amplitude, which plays a particularly important role in rare B_c decays. The $B_c \to D^*$ transition form factors are adopted from the covariant confined quark model, while the WA form factors are considered within the Bethe-Salpeter approach. Using these inputs, we have studied the differential branching fraction, the FB asymmetry, the longitudinal helicity fraction, and a comprehensive set of normalized angular observables in selected 1D and 2D NP scenarios involving the WCs $C_7^{(\prime)}$, $C_9^{(\prime)}$, and $C_{10}^{(\prime)}$.

Our results show that the interplay between the PB and WA amplitudes can significantly modify the phenomenology of the $B_c^+ \to D^{*+}\ell^+\ell^-$ decay, particularly in the low-q^2 muon range. The WA contribution produces sizable effects in several observables in both the SM and the various NP scenarios and therefore should not be neglected in precision studies of this decay. In the high-q^2 muon range, the observables are also affected by LD resonance contributions, leading to visible structures around the charmonium resonances. Consequently, the regions above the dominant resonance contributions provide a comparatively cleaner environment for probing NP effects.

Among the observables considered, the differential branching ratio and the FB asymmetry exhibit strong sensitivity to NP contributions in both the 1D and 2D NP scenarios. Furthermore, in the four-fold angular distribution, several normalized angular observables, particularly $\langle I_{2c}\rangle$, $\langle I_3\rangle$, $\langle I_5\rangle$, and $\langle I_{6s}\rangle$, show pronounced deviations from their SM predictions and provide valuable complementary information on the underlying NP structure. The sensitivity of these observables arises from the NP-modified PB amplitudes and their interference with the WA contribution, making them especially useful for constraining the relevant WCs.

The comparison of different NP scenarios indicates that sizable deviations from the SM can occur in both the muon and tau channels. In particular, the τ mode often exhibits enhanced separation among the NP scenarios due to the larger lepton-mass effects entering the helicity amplitudes. This suggests that measurements involving τ leptons could enhance the discriminatory power of these observables in future experimental studies.

We also investigated correlations among the integrated observables and found that combined measurements of the branching fraction, $A_{\rm FB}$, and f_L can help distinguish between different NP scenarios and further constrain the allowed parameter space of the NP WCs. Such correlations provide complementary information beyond individual observables and may become particularly useful as experimental precision improves.

In conclusion, our analysis demonstrates that the decay $B_c^+ \to D^{*+}\ell^+\ell^-$ constitutes a phenomenologically rich and complementary probe of NP in the $b \to d\ell^+\ell^-$ sector. The sizable WA contributions, the sensitivity of several angular observables to NP scenarios, and the distinctive patterns observed in the correlation studies make this decay an attractive channel for future investigations. The observables studied in this work should be explored at future LHCb upgrades and other high-luminosity experiments, providing valuable opportunities to reveal the flavor structure of physics beyond the SM.

ACKNOWLEDGMENTS

M.A.P. and Z.A. acknowledge financial support from the Higher Education Commission (HEC) of Pakistan through Grant No. NRPU/20-15142.

APPENDIX

Appendix A: Expressions for Wilson coefficients

The expressions used for the WCs are given in Refs. [49–54].

$$
\begin{aligned}
C_7^{eff}(q^2) &= C_7 - \frac{1}{3}\left(C_3 + \frac{4}{3}C_4 + 20C_5 + \frac{80}{3}C_6\right) - \frac{\alpha_s}{4\pi}\left[(C_1 - 6C_2)F_{1,c}^{(7)}(q^2) + C_8F_8^{(7)}(q^2)\right] \\
&\quad - \frac{\alpha_s}{4\pi}\lambda_u^{(q)}(C_1 - 6C_2)\left(F_{1,c}^{7} - F_{1,u}^{7}\right), \\
C_9^{eff}(q^2) &= C_9 + \frac{4}{3}\left(C_3 + \frac{16}{3}C_5 + \frac{16}{9}C_6\right) - h(0,q^2)\left(\frac{1}{2}C_3 + \frac{2}{3}C_4 + 8C_5 + \frac{32}{3}C_6\right) \\
&\quad - h(m_b^{\rm pole},q^2)\left(\frac{7}{2}C_3 + \frac{2}{3}C_4 + 38C_5 + \frac{32}{3}C_6\right) + h(m_c^{\rm pole},q^2)\left(\frac{4}{3}C_1 + C_2 + 6C_3\right. \\
&\quad \left. + 60C_5\right) + \lambda_u^{(q)}\left[h(m_c,q^2) - h(0,q^2)\right]\left(\frac{4}{3}C_1 + C_2\right) - \frac{\alpha_s}{4\pi}\left[C_1F_{1,c}^{(9)}(q^2)\right. \\
&\quad \left. + C_2F_{2,c}^{(9)}(q^2) + C_8F_8^{(9)}(q^2)\right] - \frac{\alpha_s}{4\pi}\lambda_u^{(q)}\left[C_1(F_{1,c}^{(9)} - F_{1,u}^{(9)}) + C_2(F_{2,c}^{(9)} - F_{2,u}^{(9)})\right]
\end{aligned}
\tag{A1}
$$

CPC Accepted

$$+ \quad Y_{res}(m_b^{pole}, q^2), \tag{A2}$$

where the functions $h(m_a^{\rm pole}, q^2)$ with $q = c, b$ and $F_8^{(7,9)}(q^2)$ are defined in [50], whereas the functions $F_{1,c}^{(7,9)}(q^2)$ and $F_{2,c}^{(7,9)}(q^2)$ are given in [53] for low q^2 and in [54] for high q^2.

The function $Y_{\rm res}(q^2, m_b^{pole})$ is defined as follows,

$$Y_{\rm res}(q^2, m_b^{pole}) = -\frac{3\pi}{\alpha_e^2}\Bigg[C(m_b^{pole}) \sum_{V_i=J/\psi,\psi(2S),\ldots} \frac{m_{V_i} B(V_i \to \ell^+\ell^-)\Gamma_{V_i}}{q^2 - m_{V_i}^2 + i m_{V_i}\Gamma_{V_i}} - \lambda_u B(0,\hat{s})(3C_1(m_b^{pole}) + C_2(m_b^{pole})) \times \sum_{V_j=\rho,\omega,\phi} \frac{m_{V_j} B(V_j \to \ell^+\ell^-)\Gamma_{V_j}}{q^2 - m_{V_j}^2 + i m_{V_j}\Gamma_{V_j}}\Bigg]. \tag{A3}$$

Here, $\hat{s} = q^2/m_b^2$ and $\hat{m}_c = m_c/m_b$, with $m_b = 4.8\,\text{GeV}$ and $m_c = 1.6\,\text{GeV}$, and $C(m_b^{pole}) = 3C_1(m_b^{pole}) + C_2(m_b^{pole}) + 3C_3(m_b^{pole}) + C_4(m_b^{pole}) + 3C_5(m_b^{pole}) + C_6(m_b^{pole})$. At next-to-leading order, the WCs at the QCD renormalization scale $m_b^{pole} = m_b$ are taken to be $C_1 = -0.175$, $C_2 = 1.076$, $C_3 = 1.258$, $C_4 = -3.279$, $C_5 = 1.112$, $C_6 = -3.634$, $C_7 = -0.302$, $C_8 = -0.148$, $C_9 = 4.232$, and $C_{10} = -4.410$ [63].

Table 5. The masses, total widths, and dileptonic widths of the intermediate vector mesons used in $Y_{res}(m_b^{pole}, q^2)$. These values are taken from the PDG [58].

V_i	m_{V_i} (GeV)	Γ_{V_i} (MeV)	$B(V_i \to \ell^+\ell^-)$ where $\ell = e,\mu$
ρ	0.775	149	4.635×10^{-5}
ω	0.783	8.68	7.380×10^{-5}
ϕ	1.019	4.249	2.915×10^{-4}
J/ψ	3.097	0.093	5.966×10^{-2}
$\psi(2S)$	3.686	0.294	7.965×10^{-3}

Appendix B: Phase structure of the amplitudes

For completeness, we summarize the phase structure of the amplitudes retained in the present calculation. For a given helicity λ, the decay amplitude can be organized schematically as

$$\mathcal{A}_\lambda(q^2) = V_{tb}V_{td}^*\left[\mathcal{H}_{\lambda,t}^{\rm SD}(q^2) + \mathcal{H}_{\lambda,t}^{\rm LD}(q^2) + \mathcal{H}_\lambda^{\rm NP}(q^2)\right] + V_{ub}V_{ud}^*\left[\mathcal{H}_{\lambda,u}^{\rm SD}(q^2) + \mathcal{H}_{\lambda,u}^{\rm LD}(q^2)\right] + V_{cb}V_{cd}^*\mathcal{H}_\lambda^{\rm WA}(q^2). \tag{B1}$$

The CKM products in Eq. (34) determine the SM weak phases. In particular, as discussed in the main text, the relative weak phase between the dominant PB normalization and the WA contribution is $\arg[(V_{cb}V_{cd}^*)/(V_{tb}V_{td}^*)] \simeq \pi - \beta$. The terms in $C_{7,9}^{\rm eff}$ that are proportional to $\lambda_u^{(d)}$ carry the additional SM weak phase associated with $V_{ub}V_{ud}^*$.

The hadronic quantities in Eq. (34) can, in general, be written as

$$\mathcal{H}_{\lambda,k}(q^2) = \left|\mathcal{H}_{\lambda,k}(q^2)\right| e^{i\delta_{\lambda,k}(q^2)}, \tag{B2}$$

where $\delta_{\lambda,k}(q^2)$ denotes the corresponding strong phase. In the PB contribution, the perturbative functions entering $C_{7,9}^{\rm eff}$ can acquire imaginary (absorptive) parts through their loop functions [50, 53, 54]. The LD contribution induces an additional, more pronounced q^2-dependent phase through the Breit–Wigner factors appearing in $Y_{\rm res}$,

$$\delta_V(q^2) = \arg\left[\frac{1}{q^2 - m_V^2 + i m_V\Gamma_V}\right], \tag{B3}$$

which varies rapidly as q^2 crosses a vector-meson pole. The WA contribution has its own q^2-dependent hadronic phase because the BS form factors are complex-valued functions,

$$T_{\rm ann}(q^2) = \mathrm{Re}\,T_{\rm ann}(q^2) + i\,\mathrm{Im}\,T_{\rm ann}(q^2), \quad \delta_{\rm WA}(q^2) = \arg T_{\rm ann}(q^2), \tag{B4}$$

as obtained in Ref. [42].

Consequently, the phase differences relevant to PB–WA and PB–LD interference are not constant across the dilepton-mass spectrum. For the CP-averaged observables considered in this work, an interference term between two contributions i and j schematically depends on

$$2|\mathcal{A}_i||\mathcal{A}_j|\cos\left[\delta_i(q^2) - \delta_j(q^2)\right]\cos\left(\phi_i - \phi_j\right), \tag{B5}$$

where ϕ_i and ϕ_j denote the corresponding weak phases. This form explicitly shows why the interference pattern varies with q^2, even when the CKM weak-phase difference is fixed. The preceding discussion summarizes the phase structure included in the present calculation; possible additional nonfactorizable phases from final-state

CPC Accepted

interactions or rescattering beyond the adopted BS treatment are not included.

Appendix C: Direct CP asymmetry

Fig. 11 depicts the direct CP asymmetry in the $B_c^+ \to D^{*+}\ell^+\ell^-$ decay for the low- and high-q^2 bins in the SM. The corresponding bin-averaged values in the low- and high-q^2 muon bins are $\langle A_{\rm CP}\rangle_{\rm low} = -0.033$ and $\langle A_{\rm CP}\rangle_{\rm high} = -0.002$, respectively. These values differ significantly from those reported in Ref. [43], in which the CP asymmetry is computed using only the PB relative weak phases ($\lambda_u^{(d)} = V_{ub}V_{ud}^*/(V_{tb}V_{td}^*)$). Computing CP asymmetries for all other observables is beyond the scope of the present study; therefore, we leave this topic for future work.

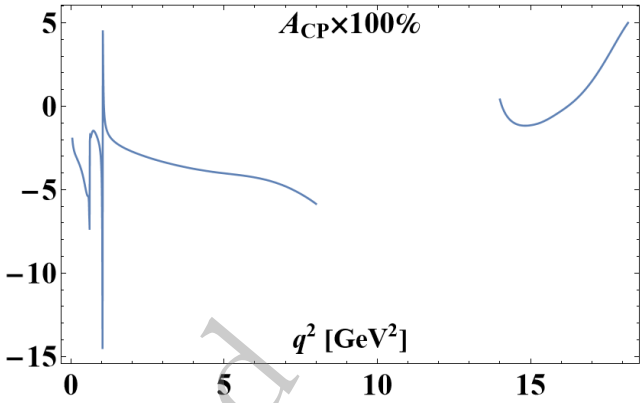

Fig. 11. SM predictions for the direct CP asymmetry $A_{\rm CP}(q^2)$ in the decay $B_c^+ \to D^{*+}\ell^+\ell^-$ for the low- and high-q^2 muon regions.

CPC Accepted

References

[1] N. Cabibbo, Phys. Rev. Lett. **10**, 531 (1963)
[2] M. Kobayashi and T. Maskawa, Prog. Theor. Phys. **49**, 652 (1973)
[3] R. Aaij *et al.* (LHCb Collaboration), Phys. Rev. Lett. **131**(5), 051803 (2023), arXiv: 2212.09152[hep-ex]
[4] R. Aaij *et al.* (LHCb Collaboration), Phys. Rev. Lett. **125**(1), 011802 (2020), arXiv: 2003.04831[hep-ex]
[5] R. Aaij *et al.* (LHCb Collaboration), JHEP **11**, 043 (2021), arXiv: 2107.13428[hep-ex]
[6] R. Aaij *et al.* (LHCb Collaboration), arXiv: 2604.21987[hep-ex]
[7] R. Aaij *et al.* (LHCb Collaboration), JHEP **10**, 034 (2015), arXiv: 1509.00414[hep-ex]
[8] J. P. Lees *et al.* (BaBar Collaboration), Phys. Rev. D **88**(3), 032012 (2013), arXiv: 1303.6010[hep-ex]
[9] J. T. Wei *et al.* (Belle Collaboration), Phys. Rev. D **78**, 011101 (2008), arXiv: 0804.3656[hep-ex]
[10] I. Adachi *et al.* (Belle, Belle-II Collaboration), Phys. Rev. Lett. **133**(10), 101804 (2024), arXiv: 2404.08133[hep-ex]
[11] R. Aaij *et al.* (LHCb Collaboration), JHEP **07**, 020 (2018), arXiv: 1804.07167[hep-ex]
[12] E. Kou *et al.*, PTEP **2019**(12), 123C01 (2019), arXiv: 1808.10567[hep-ex]
[13] S. Ishaq, F. Munir, and I. Ahmed, JHEP **07**, 006 (2013)
[14] Z. R. Huang, M. A. Paracha, I. Ahmed *et al.*, Phys. Rev. D **100**(5), 055038 (2019), arXiv: 1812.03491[hep-ph]
[15] F. Munir, S. Ishaq, and I. Ahmed, PTEP **2016**(1), 013B02 (2016), arXiv: 1511.07075[hep-ph]
[16] F. Munir Bhutta, Z. R. Huang, C. D. Lü *et al.*, Nucl. Phys. B **979**, 115763 (2022), arXiv: 2009.03588[hep-ph]
[17] F. M. Bhutta, A. Rehman, M. J. Aslam *et al.*, Phys. Rev. D **111**(9), 095011 (2025), arXiv: 2410.20633[hep-ph]
[18] D. Das, B. Kindra, G. Kumar *et al.*, Phys. Rev. D **99**(9), 093012 (2019), arXiv: 1812.11803[hep-ph]
[19] M. K. Mohapatra and A. Giri, Phys. Rev. D **104**(9), 095012 (2021), arXiv: 2109.12382[hep-ph]
[20] N. Rajeev, N. Sahoo, and R. Dutta, Phys. Rev. D **103**(9), 095007 (2021), arXiv: 2009.06213[hep-ph]
[21] R. Aaij *et al.* (LHCb Collaboration), Phys. Rev. Lett. **108**, 251802 (2012), arXiv: 1204.0079[hep-ex]
[22] R. Dutta, Phys. Rev. D **100**(7), 075025 (2019), arXiv: 1906.02412[hep-ph]
[23] M. K. Mohapatra, N. Rajeev, and R. Dutta, Phys. Rev. D **105**(11), 115022 (2022), arXiv: 2108.10106[hep-ph]
[24] M. Zaki, M. A. Paracha, and F. M. Bhutta, Nucl. Phys. B **992**, 116236 (2023), arXiv: 2303.01145[hep-ph]
[25] Y. S. Li and X. Liu, Phys. Rev. D **108**(9), 093005 (2023), arXiv: 2309.08191[hep-ph]
[26] Q. M. U. Salam, I. Ahmed, R. Khalid *et al.*, J. Phys. G **52**(4), 045003 (2025), arXiv: 2411.00912[hep-ph]
[27] C. Q. Geng, C. W. Hwang, and C. C. Liu, Phys. Rev. D **65**, 094037 (2002), arXiv: hep-ph/0110376[hep-ph]
[28] K. Azizi, F. Falahati, V. Bashiry *et al.*, Phys. Rev. D **77**, 114024 (2008), arXiv: 0806.0583[hep-ph]
[29] K. Azizi and R. Khosravi, Phys. Rev. D **78**, 036005 (2008), arXiv: 0806.0590[hep-ph]
[30] A. Faessler, T. Gutsche, M. A. Ivanov *et al.*, Eur. Phys. J. direct **4**(1), 18 (2002), arXiv: hep-ph/0205287[hep-ph]
[31] H. M. Choi, Phys. Rev. D **81**, 054003 (2010), arXiv: 1001.3432[hep-ph]
[32] W. F. Wang, X. Yu, C. D. Lü *et al.*, Phys. Rev. D **90**(9), 094018 (2014), arXiv: 1401.0391[hep-ph]
[33] U. O. Yilmaz, Phys. Rev. D **85**, 115026 (2012), arXiv: 1204.1261[hep-ph]
[34] D. Ebert, R. N. Faustov, and V. O. Galkin, Phys. Rev. D **82**, 034032 (2010), arXiv: 1006.4231[hep-ph]
[35] P. Maji, S. Mahata, P. Nayek *et al.*, Chin. Phys. C **44**(7), 073106 (2020), arXiv: 2003.12272[hep-ph]
[36] P. Maji, S. Biswas, P. Nayek *et al.*, PTEP **2020**(5), 053B07 (2020), arXiv: 2003.07041[hep-ph]
[37] M. A. Paracha, I. Ahmed, and M. J. Aslam, Phys. Rev. D **84**, 035003 (2011), arXiv: 1101.2323[hep-ph]
[38] I. Ahmed, M. A. Paracha, M. Junaid *et al.*, arXiv: 1107.5694[hep-ph]
[39] A. Ahmed, I. Ahmed, M. A. Paracha *et al.*, arXiv: 1108.1058[hep-ph]
[40] Z. Aarfi, Q. M. U. Salam, I. Ahmed *et al.*, Eur. Phys. J. C **86**(5), 456 (2026), arXiv: 2602.10903[hep-ph]
[41] M. A. Ivanov, J. N. Pandya, P. Santorelli *et al.*, Phys. Rev.

D **110**, 096003 (2024), arXiv: 2404.15085[hep-ph]
[42] W. L. Ju, G. L. Wang, H. F. Fu *et al*., JHEP **04**, 065 (2014), arXiv: 1307.5492[hep-ph]
[43] U. Dey and S. Nandi, arXiv: 2509.19445[hep-ph]
[44] B. Wu, G. L. Yu, Z. G. Wang *et al*., arXiv: 2412.00515[hep-ph]
[45] Y. K. Huang, Y. L. Shen, C. Wang *et al*., Phys. Rev. Lett. **134**(9), 091901 (2025), arXiv: 2403.11258[hep-ph]
[46] R. Bause, H. Gisbert, M. Golz *et al*., Eur. Phys. J. C **83**(5), 419 (2023), arXiv: 2209.04457[hep-ph]
[47] N. Farooq, M. Zaki, M. A. Paracha *et al*., Chin. Phys. C **48**(10), 103107 (2024), arXiv: 2407.00520[hep-ph]
[48] Z. Aarfi, Q. M. U. Salam, I. Ahmed *et al*., PTEP **2025**(12), 123B10 (2025), arXiv: 2506.20446[hep-ph]
[49] D. Du, A. X. El-Khadra, S. Gottlieb *et al*., Phys. Rev. D **93**(3), 034005 (2016), arXiv: 1510.02349[hep-ph]
[50] M. Beneke, T. Feldmann, and D. Seidel, Nucl. Phys. B **612**, 25 (2001), arXiv: hep-ph/0106067[hep-ph]
[51] C. Bobeth, M. Misiak, and J. Urban, Nucl. Phys. B **574**, 291 (2000), arXiv: hep-ph/9910220[hep-ph]
[52] H. H. Asatrian, H. M. Asatrian, C. Greub *et al*., Phys. Lett. B **507**, 162 (2001), arXiv: hep-ph/0103087[hep-ph]
[53] H. H. Asatryan, H. M. Asatrian, C. Greub *et al*., Phys. Rev. D **65**, 074004 (2002), arXiv: hep-ph/0109140[hep-ph]
[54] C. Greub, V. Pilipp, and C. Schupbach, JHEP **12**, 040 (2008), arXiv: 0810.4077[hep-ph]
[55] W. L. Ju, G. L. Wang, H. F. Fu *et al*., JHEP **09**, 171 (2015), arXiv: 1407.7968[hep-ph]
[56] Z. D. Duan, J. P. Wang, R. H. Li *et al*., JHEP **09**, 160 (2025), arXiv: 2412.20458[hep-ph]
[57] H. Y. Cheng, C. K. Chua, and A. Soni, Phys. Rev. D **71**, 014030 (2005), arXiv: hep-ph/0409317[hep-ph]
[58] R. L. Workman *et al*. (Particle Data Group), PTEP **2022**, 083C01 (2022)
[59] S. Navas *et al*. (Particle Data Group), Phys. Rev. D **110**(3), 030001 (2024)
[60] A. Crivellin, C. Greub, D. Müller *et al*., Phys. Rev. Lett. **122**(1), 011805 (2019), arXiv: 1807.02068[hep-ph]
[61] C. Bobeth, A. J. Buras, A. Celis *et al*., JHEP **04**, 079 (2017), arXiv: 1609.04783[hep-ph]
[62] A. D'Alise, G. Fabiano, D. Frattulillo *et al*., Nucl. Phys. B **1006**, 116631 (2024), arXiv: 2403.17614[hep-ph]
[63] G. Buchalla, A. J. Buras, and M. E. Lautenbacher, Rev. Mod. Phys. **68**, 1125 (1996), arXiv: hep-ph/9512380[hep-ph]

CPC Accepted